VALUE OF PERI-URBAN AND SMALL-SCALE MANGROVE FORESTS IN THE PEARL RIVER ESTUARY AS FISH HABITATS
(MEEF2019002 & MEEF2019002A)

Completion Report

Lee, S.Y. *The Chinese University of Hong Kong, Hong Kong SAR* and

Uwe Grueters *Justus Liebig University of Giessen, Germany*

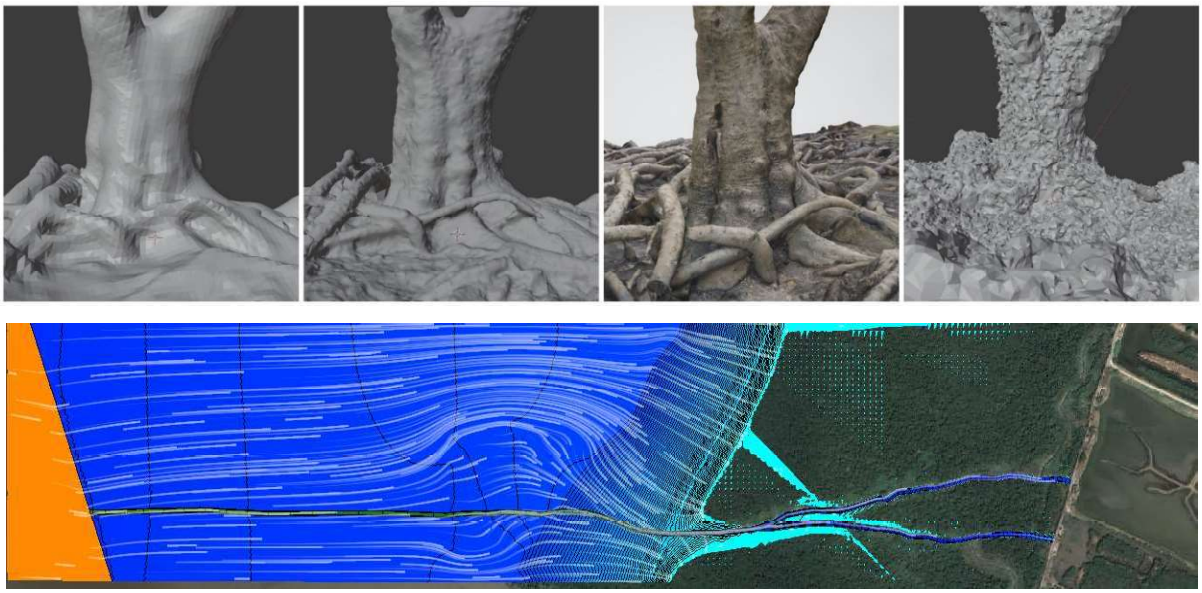

A Study Funded by the

Marine Ecology Enhancement Fund, Hong Kong Airport Authority

February 2022

VALUE OF PERI-URBAN AND SMALL-SCALE MANGROVE FORESTS IN THE PEARL RIVER ESTUARY AS FISH HABITATS (MEEF2019002 & MEEF2019002A)

Completion Report

Executive Summary

We conducted a study of the role small mangrove patches play as nursery sites for juvenile fish. The study comprised the following components: (1) use of small mangrove patches by juvenile fish; (2) developing a simple but effective method for constructing digital 3-dimensional models of mangrove structures that may underpin the nursery role; (3) conduct context-sensitive realistic experiments to evaluate the importance of mangrove structural complexity in protecting juvenile fish from their predators; and (4) develop an individual-based model in describing the use of mangrove structures by juvenile fish.

Underwater video surveys confirmed the use of the local small-scaled mangroves by a wide range of juvenile fish species. We evaluated the efficacy of three methods for scanning and constructing digital 3-D models of individual mangrove trees using three methods, namely, the Kinect RGB sensor, photogrammetry, and a laser scanner. Both the Kinect and photogrammetry were able to capture the structural complexity of the mangrove trees satisfactorily, with the latter approach most cost-effective in delivering the most realistic digital model.

We selected three models for printing to produce life-size mangrove patches. The models have different levels of structural complexity and were used in mesocosm experiments for assessing the role of mangrove structure in the interaction between juvenile fish and their predators. Using two species of small fish and a predator common in local mangroves, the effects of water level, mangrove complexity, and fish species on the interaction were assessed using video-recorded experiments. Both fish species, water level, and complexity had a significant effect on mortality of the small fish.

Central achievements have been made in developing an individual-based model (IBM) to simulate the use of small-scaled mangrove forests by juvenile fish communities, called InMANGROVE: (1) translation of the InSTREAM model to (Geo-)MASON/Java; (2) successful evaluation of correct code translation with debugging, testing (Junit, Mockito) and visual comparison techniques; (3) deriving mangrove structural complexity of aerial root networks in the Mai Po Nature Reserve using allometric relationships; (4) incorporation of tidal scheduling in the model including routines for harmonic tide prediction; and (5) conducting hydrodynamic simulations with HEC-RAS to derive rating curves between tidal stage and water depths/velocities for Mai Po mangroves.

Disclaimer

"Any opinions, findings, conclusions or recommendations expressed in this report do not necessarily reflect the views of the Marine Ecology Enhancement Fund or the Trustee."

Table of Contents

List of Figures

List of Tables

Overview of the Project

This project aims to investigate the importance of peri-urban, small-scale mangrove patches in the Pearl River estuary (PRE) in supporting fishery production through the provision of nursery environments. The capacity for coastal wetlands such as mangrove forests to act as nursery sites is thought to depend on (a) the habitat structural complexity; and /or (b) the provision of food; these dependencies are respectively termed the "protection" and "food" hypotheses. Despite that these hypotheses having been proposed for decades, little direct evidence is available for assessing their application to mangrove ecosystems, especially small patches in peri-urban settings. This study tests the protection hypothesis using small mangrove patches in Hong Kong and the PRE.

The specific work packages (WP) of the project are:

1. To assess the value of peri-urban small-scale mangrove forests in the Pearl River estuary as habitat for juvenile fish. We survey the types and species of fish that utilize mangrove patches using underwater video cameras and nets.
2. To understand the importance of mangrove forest structural complexity for supporting juvenile fish use of the habitat. We conduct *ex situ* predation experiments using 3D printed real-size mangrove structure and observe how juvenile prey fish utilize complex mangrove structures as protection from predation by larger fish.
3. To forecast juvenile fish behaviour in realistic mangrove structures under different environmental constraints using Individual Based Models (IBM). We are constructing the IBMs in a collaboration with the University of Giessen in Germany. The results of the models will be validated by the results of WP2.

Phase I (WP1 and WP2, Year 1) of the project focuses on the field and laboratory components whereas Phase II (WP3, Year 2) of the project focuses on the modelling component of the project. Based on the above findings, we recommend ecologically sound options for the management and restoration of mangrove habitats in the PRE.

Despite the challenges we are facing due to COVID-19 pandemic, we have successfully completed most of the project objectives we set, from conducting surveys using video cameras to understand the fish abundance and diversity in various mangrove patches in Hong Kong and PRE, scanning and printing real-size mangrove tree models, conducting predation experiments, and constructing an Individual Based Model. We are currently conducting more predation experiments using the models we have printed and the fish we have collected from the surveys and refining the model for predicting fish behaviour.

Project background

Mangrove forests are highly productive ecosystems (Alongi 2009) that thrive on tropical estuarine coastlines, where the combined conditions of warm sea temperature, reduced seawater salinity and the supply and accumulation of sediments create conditions for

their dominance. The current area of mangroves stands at *ca.* 135,000 km^2 (Global Mangrove Watch 2021), which is a small percentage of their extent before decades of widespread losses to urbanization, coastal aquaculture and agriculture (UNEP 2014). Mangrove forests in Asia, for example, suffered annual losses of 1-2% between 1980 and 2000 (FAO 2007) but the rate of decline has since been reduced to <1% (Richards and Friess 2016). Mangrove structures such as aerial roots and tree trunks, particularly of shrubby species, create a highly complex spatial environment both in terms of the number of structures and their three-dimensional arrangement (Figure 1). These complex tree structures underpin numerous functions and services offered by mangrove ecosystems, e.g., protecting coastlines from storm surges, trapping sediment and particulate carbon, and sustaining fisheries by supporting the larval and juvenile stages of fish and crustaceans of high commercial and ecological importance (Kamal et al. 2017, Lee et al. 2014).

Figure 1. Complexity of mangrove structures. (A) The shrubby local mangrove *Aegiceras corniculatum* offers a spatially complex environment on an otherwise featureless tidal flat habitat at Lai Chi Wo, NE Hong Kong. (B) The aerial stilt roots of *Rhizophora stylosa* and the pneumatophores of *Avicennia marina* can effectively dampen water flow, trap sediments, and provide refuge to animals from extreme physical conditions or predators.

One of the main services recognised for tropical mangroves is to act as nursery sites for juvenile nekton (free-swimming fish, crustaceans) but the mechanism of this benefit is unclear. Early speculations on this function were based on indirect evidence, such as correlations between mangrove area and coastal fish production (Manson et al. 2005). Mangrove structures are hypothesized to offer habitats abundant in food as well as reduced

predation pressure (Laegdsgaard and Johnson 2001, Sheaves et al. 2015), but this notion is still controversial as (1) data on the dynamics and drivers of juvenile fish use of mangroves are scarce; and (2) supportive evidence is either correlational in nature or from experiments that lack realism. Drivers that may influence juvenile nekton use of mangrove forests may be environmental, such as the level of general disturbance, or scent (e.g., Huijbers et al. 2008, Natin and Lee 2018). While these factors may guide or repel juvenile nekton to or from mangroves, ecological factors such as the structural characteristics of the forest and food availability are likely more important as positive drivers for mangrove use. However, the latter category of drivers is poorly understood.

Studies in Australia have revealed the dynamics of fish use of mangroves (Laegdsgaard and Johnson 1995, Robertson and Duke 1990a, b) but their results are largely inapplicable to smaller and remnant systems such as those in the Pearl River Estuary (PRE), where the levels of general human disturbance, the diversity of chemical cues and the size and structure of the mangrove forests are distinctly different (Brooker et al. 2020). With continued urbanization, the mangrove forests in many peri-urban estuaries have declined in area and became increasingly fragmented. Change in mangrove seascape metrics is known to correlate with coastal fish catch (Meynecke et al. 2008). To what extent these small-scale mangrove patches are still able to support use by juvenile fish as nursery sites is of both academic as well as management significance. This study funded by a grant from the Marine Ecology Enhancement Fund (MEEF) attempted to address this question by using of a novel approach: to conduct realistic controlled experiments on protection of juvenile fish from predators using mangrove structures captured and reproduced through 3D scanning and 3D printing technology.

The PRE is the exit point for river-borne materials (e.g., nutrients, sediments, pollutants) from the largest metropolis in the world (population >65 million). Over the past three decades, PRE has experienced extensive land reclamation (Wei et al. 2021) and severe water pollution due to the high population density and rapid industrial and agricultural development (Zhao et al. 2020). Once lined with luxuriant mangrove forests, the coastline of the PRE is now highly modified and strongly disturbed, with only relatively small patches of mangrove forests remaining to support the many potential ecosystem services of these productive ecosystems (Lee 2022). At an overall area of <500 ha, the forests in inner Deep Bay comprising the Mai Po Nature Reserve and the Futian Nature Reserve are already the largest remaining mangroves in the Pearl River Delta. The PRE also used to be a major

spawning ground for many commercially important species such as the yellow croaker (*Larimychthys polyactis*), the Japanese sea perch (*Lateolabrax japonicus*), and the giant perch (*Lates calcarifer*), some of are known to use the mangrove forests as nursery or feeding sites (Sheaves et al. 2007). To what extent these peri-urban and small-scale mangrove patches are able to function as habitat for juvenile fish is of both academic as well as management significance. While continuous urbanization has reduced much of the original luxurious mangrove forests in the PRE to small remnant patches, these patches may still perform a key role in estuarine function (Curnick et al. 2019).

The drivers that determine use of mangrove forests as habitats of juvenile fish have been subjects of controversy. While factors operating at the seascape level may be important (Sheaves et al. 2015), three non-exclusive hypotheses on local habitat-level drivers have been proposed (Laegdsgaard & Johnson 2001; Nagelkerken 2009). First, the *food hypothesis* proposes that since mangrove forests are highly productive, juvenile fish that are less effective predators but more vulnerable as prey in open waters, may have higher chance of success to obtain food in mangroves. Second, the *protection hypothesis* states that the generally high turbidity as well as high structural complexity of the mangrove environment will enhance juvenile fish survival from visual, 'pursuit-type' predators. Third, the *energy hypothesis* proposes that juvenile fish can obtain respite from extreme environmental conditions, e.g., thermal stress, in the shaded mangrove habitat. The first two hypotheses are of most interest to fish ecologists but tests on their validity have been hampered by the lack of appropriate technology that enables measurement in the generally challenging mangrove environment – the wet-dry tidal inundation cycle, the high turbidity and the high spatial complexity of the habitat all make sampling and context-sensitive and realistic measurement difficult.

Research regarding the functions of complex mangrove tree structures have therefore resorted to invasive harvesting of tree pneumatophores (e.g., Horstman et al. 2018) or utilizing simplistic mimics with little resemblance to actual mangrove tree structures (e.g., circular cylinders and cones in Mazda et al. (1997); wooden sticks in Laegdsgaard and Johnson (2001); PVC pipes in de la Moriniere et al. (2004) and Nagelkerken et al. (2010)). Meanwhile, traditional non-invasive methods to reconstruct realistic complex structures, such as small coral colonies, typically relied on using a stationary 3D scanner while manually rotating the object around on a fixed location (e.g., Gutierrez-Heredia et al. 2015; Reichert et al. 2016). While it is possible to conduct this method with minimal harm toward coral

colonies (Reichert et al. 2016), it is not possible to non-destructively scan or extract mangrove tree structures that are typically large, deeply rooted in the ground, and may comprise of isolated components that are connected only belowground. Realistic reconstruction of their complex structures was only made possible by utilizing handheld scanners, such as the Xbox Kinect (Kamal et al. 2014). The capture of digital models and their subsequent reconstruction through 3D printing of habitat-forming species such as coral colonies and mangrove trees may allow context-sensitive observations and experimentations that can shed light on previously obscure ecological processes.

Despite all the progress made with the Xbox Kinect in understanding mangrove structural complexity (Kamal et al. 2014; Vorsatz et al. 2021) and its ability in trapping sediment (Kamal et al. 2017), the mangrove trees generated by this technique had not been applied for experimentations related to their use as refuge for juvenile fish (Laegdsgaard & Johnson 2001; Nagelkerken 2009). Moreover, the discontinuation of the Xbox in 2015 engendered the need to find a new method to efficiently reproduce high-quality mangrove structures for ecological research purposes.

In this study, we tested three different 3D scanning methods to reproduce mesh models of mangrove tree structures: an Xbox Kinect for Windows, structure from motion (SfM) photogrammetry, and a handheld mobile laser scanner GeoSLAM ZEB Revo RT. We then determined the best technique for the mangrove structure reconstruction based on each model's structural complexity metrics and its resemblance of the copied tree. The models generated by this technique were then utilized for several ecological research purposes, namely through 3D printing for manipulative experiments in mesocosms, and modelling of fish use of the habitat based on actual 3D structure using individual-based modelling (IBM) approaches.

Materials and Methods

Work Package 1 (WP1) Juvenile fish use of small peri-urban mangroves

Fish assemblages were surveyed in the mangrove patches of Ting Kok (TK) and Lai Chi Wo (LCW) in the northeast, and Shui Hau (SH) in the southwest of Hong Kong. Mainland Chinese study locations mentioned on the project proposal were not used due to travel restrictions during the COVID-19 pandemic. Fish surveys were conducted with a combination of underwater video cameras and various nets, including fyke nets, centipede traps, and umbrella traps (Figure 2). Underwater cameras have been successfully used for this purpose in mangroves (Peng et al. 2017) but due to the expected high turbidity in the PRE, the use of nets was necessary to complement data collected using video cameras.

Figure 2. **Nets used in fish surveys.** Top: project members pulling a net in Shui Hau, bottom left: an umbrella net, bottom right: a centipede trap).

We deployed stationary centipede traps and umbrella traps in several positions along the mangrove patches in SH and TK. These traps could effectively sample nekton in mangrove forests as they are flexible enough to fit in any space available among the trees and can also be deployed at very shallow water depths (< 15 cm). We also dragged fyke nets along the mangrove streams in SH, which were narrow and deep enough (~1 m) for efficient capture of most fish species. No fish were captured using nets but only cameras were used in LCW due to its status as a Marine Protected Area (MPA), while fyke nets were not dragged in TK as its flooded portion were too open for effective usage of this method. Three to six underwater cameras were tied to strong fixed structures (tree trunk, tree branch, or *Avicennia marina* pneumatophores) facing either mangrove patches or the sea. Videos started recording when the tides were rising (~1.4 – 1.5 m high above Chart Datum) to observe fish swimming into the mangrove patches.

Work Package 2 (WP2) Drivers for use of mangroves by juvenile fish

3D scanning methods

While we originally planned to use GeoSLAM ZEB Revo RT to scan the mangrove structures, preliminary tests using this tool did not produce desirable outcomes. Thus, we tested three different 3D scanning techniques to identify the best method for scanning of mangrove structures. These methods included: (1) scanning digital mesh with an Xbox Kinect V1, a gaming device with an RGB camera and a depth sensor; (2) reconstructing digital 3D mesh from photographs taken on smartphones using Meshlab, a free open-source photogrammetry software; and (3) capturing point-cloud data using GeoSLAM ZEB Revo RT, a handheld mobile laser scanner (Figure 3). Seven mangrove tree scans were taken with all methods consecutively for three times when the tides were low in each site during overcast days, early mornings, and dusks to limit 'holes' in scanned mesh objects. These 'holes' appeared more frequently when direct sunlight hit tree surfaces and drastically changed the temperature of patches of exposed areas (Kamal et al., 2014). A PVC pipe (L = 1 m, d = 2.5 cm) was positioned in relative proximity to the tree to aid with scaling and ground truthing of tree parameters.

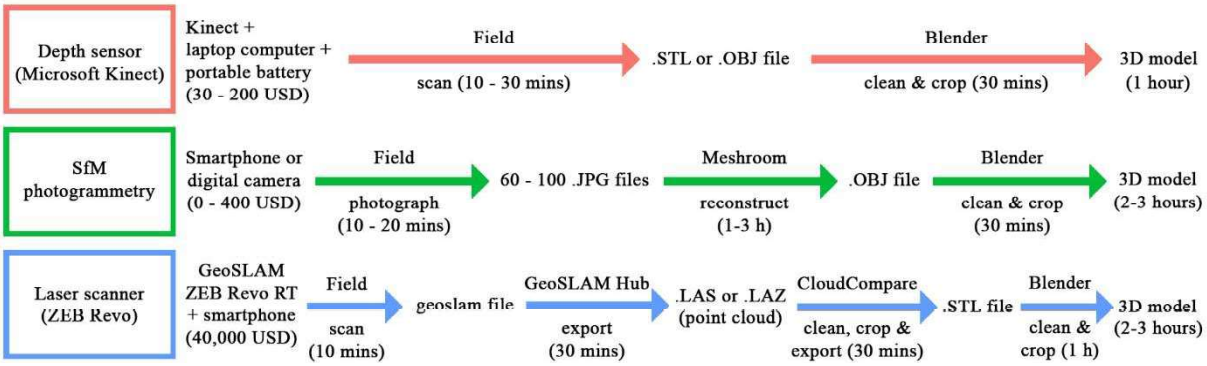

Figure 3. Summary of scanning workflow leading to the construction of 3D models using three unique approaches.

Six common mangrove tree species were scanned from SH, TK and LCW: *Aegiceras corniculatum*, *Excoecaria agallocha*, *Kandelia obovata*, *Bruguiera gymnorhiza*, *Avicennia marina*, and *Sonneratia apetala* (Table 1). Trees were chosen for scanning based on their structural complexity and accessibility, i.e., the amount of space available for researchers to move around, close to, and back from the trees. As the functions and services of interest (e.g., role of tree roots as nursery sites or for trapping of sediment and organic matter) relate fundamentally only to the submerged portion of the tree during high tide, theoretically the scanning can be conducted at all locations where the researcher can access the space around the lower trunk and aerial root structures. We were also primarily interested in how individual trees might be able to provide spatial refuge to juvenile fish from predators.

Table 1. Comparison of six mangrove tree species of different structures and complexities scanned in three sites in Hong Kong.

Species	Main trunk characteristics	Root structure	Habitats
Aegiceras corniculatum	Multiple trees that group into clusters that grow prostrate. Often brown or grey in colour, covered by epibionts such as oysters or barnacles.	Often bare, although few knee roots may surround main trunks	TK, LCW, SH
Excoecaria agallocha	One main light-coloured trunk, smooth in texture.	Long and branching, often exposed aerial roots	LCW, SH
Kandelia obovata	One main small to medium-sized and brown-coloured trunk, smooth texture.	Short prop roots, with occasional curly aerial roots	TK, LCW, SH
Bruguiera gymnorhiza	One large main trunk, tall and dark in colour.	Numerous short prop roots/knee joints	LCW
Avicennia marina	One main trunk, often short and pale with bushy canopy, usually covered by oyster colonies. Local variety often prostrate in growth form.	Numerous short and thin pneumatophores surrounding trunk	TK, LCW, SH
Sonneratia apetala	One main trunk, tall and dark in colour.	Numerous long, conical, and wide pneumatophores, often far away from main trunk	SH

Xbox Kinect

An Xbox Kinect V1, connected to a laptop computer (Dell Latitude Rugged 7414) and a 12V lithium-ion battery pack, was moved in a sine-wave shape gently around a mangrove tree to obtain a 360° scan while maintaining around one meter distance from the tree (Fig. 4). The software Kinect Fusion Explorer-WPF within the companion program Kinect for Windows Software Development Kit (SDK) v1.8.0 was downloaded on the laptop computer from the Microsoft website (https://developer.microsoft.com/en-us/windows/kinect/) and used to visualize live scanning processes to the researchers. Following the methods developed by Kamal et al. (2014), scanning parameters were set to capture the 3D object at 256 × 256 × 256 (x, y, z) voxel resolution with 0.35 - 3.50 m depth threshold, while maximum volume integration weight and volume voxels per meter were set

to 0 and 256, respectively. After the scanning process was completed, the 3D object was saved as a .STL or .OBJ file.

Figure 4. **The Xbox Kinect sensor**. Project members scanning an *Aegiceras corniculatum* patch using a Kinect sensor. The sensor was plugged to a waterproof laptop computer, which showed the scanning process in real-time.

Photogrammetry

About 70 to 100 pictures of each mangrove tree were taken from different sides, angles, and distances using a smartphone (Samsung Galaxy S9+ with a 12-MP rear camera) for 3D reconstruction with SfM photogrammetry. We started taking pictures one meter away from the tree standing up and moved one step to the side until circled around the tree. We then took one step closer and repeated the photo taking actions. Depending on the complexity of the tree, we also repeated taking pictures while crouching down and changing the angle of our smartphones. Close-up photographs of the tree structures (10 – 20 cm) were taken afterward to ensure the optimization of textures generated. They were taken haphazardly, but attention was given to take every single nook and cranny from different angles in at least five pictures to ensure comprehensive coverage.

Meshroom v2019.2.0, a free and open-source photogrammetry software (https://alicevision.org/#meshroom), was used for digital mesh reconstruction (Figure 5). To satisfy Meshroom's graphics processing unit (GPU) requirement (at least an NVIDIA CUDA-enabled GPU), a Windows 10 Home 64-bit desktop computer with NVIDIA GeForce

RTX 2060 GPU was used. Images were imported to the software and underwent a series of photogrammetric pipeline: feature extraction, image matching, feature matching, structure from motion, depth maps estimation, meshing, texturing, and localization (AliceVision 2018). The resulting mesh was saved to an auto-generated folder in the .OBJ format.

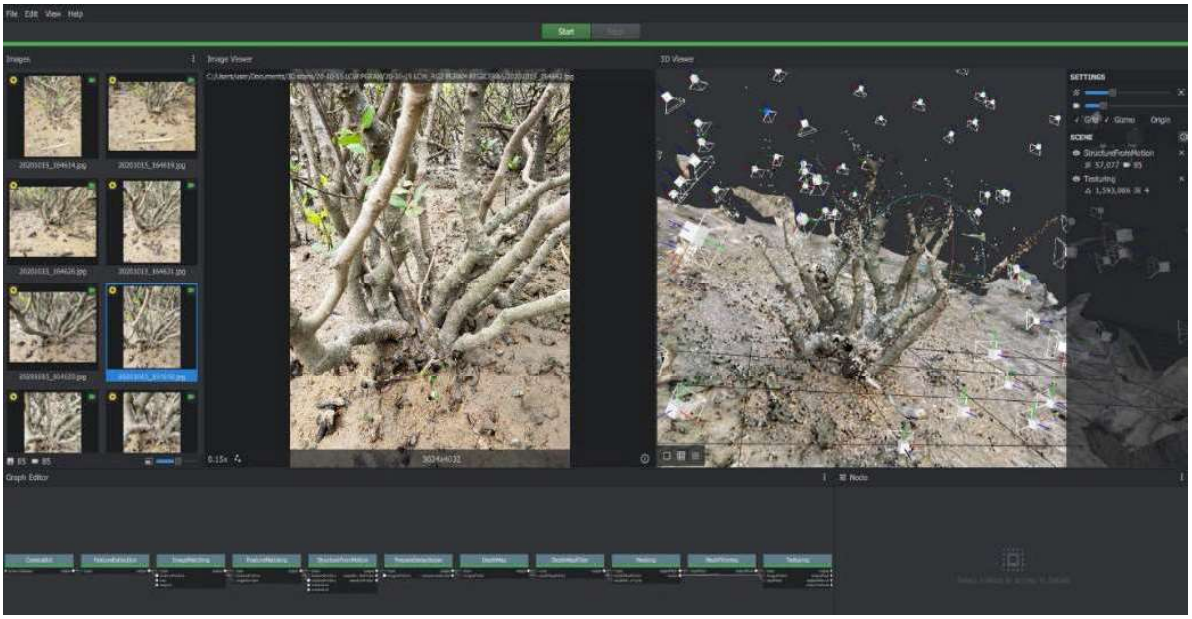

Figure 5. Meshroom interface during mesh reconstruction using 85 photographs of a tree. Left and centre screens show pictures of the tree, while the right screen shows the reconstructed model. White 'camera' icons above the model indicate the location of the smartphone during photo taking.

GeoSLAM ZEB Revo laser scanner

Lastly, the ZEB Revo was wirelessly connected to a smartphone to visualize the scanning event in real time, held closely at chest level, and walked around the surrounding tree(s) for two or three rounds. ZEB Revo was able to collect spatial data from almost every angle continuously while we moved around the area, but it was often necessary to crouch and point the scanner to areas of interest, e.g., complex root systems, to make sure every detail was taken into account. Point cloud data (.LAZ or .LAS) was downloaded to a computer via GeoSLAM Hub v5.3.0 (available through the purchase of ZEB Revo) and imported to the software CloudCompare v2.11.3 (2020). Noise was cleaned using the statistical outlier removal (SOR) filter (sigma = 1.0 or 3.0, depending on noise level), and a mesh model (.OBJ file) was created using the Poisson surface reconstruction command (octree depth = 12) following the computation of the model's quadric normal.

Using Blender v2.9.0, similar methods were performed on all mesh models for noise cleaning and cropping. In Object Mode, all models of each tree species were aligned in the same position at the centre of the axes along with a mesh box (dimension: 1 × 1 × 0.4 or 0.5 m, depending on the height of the models produced), which was subsequently used to cut all the models into a uniform size using the Boolean intersect modifier. In Edit Mode, all vertices disconnected from the main tree were selected using the commands CTRL+L (select linked), CTRL+I (select inverse), and were deleted. The models were then made watertight by removing non-manifold edges using the 3D-Print Toolbox add-on.

Comparison of the scanning methods

Several metrics were used to determine the best 3D scanning method for the printing of models. Area/volume ratio (AVR) and interstitial volume ratio (IVR) were calculated for all 3D models using Blender v2.9.0. AVR estimates the amount of surface area available for interaction with the environment in relation to the volume of the structure, i.e., more complex structures would have higher area to volume ratios. IVR refers to the volumetric space of interstitial gaps within the models over the amount of available space. IVR was calculated by subtracting the volume of the tree model from the volume of an additional mesh that wraps the model tightly and divided over the volume of the box used for cutting the model. The tight mesh was created using the 'shrinkwrap' modifier tool on a sphere mesh following the guidelines on Sadchatheeswaran et al. (2019). Additionally, efforts to ground truth the dimensions of the scanned models toward the actual trees were made by comparing the tree circumference at 50 cm height, or at the base for *A. marina*, which has a prostrate growth form in Hong Kong. The circumference was not measured at breast height due to the relatively small size of the trees in Hong Kong. Using the MeasureIt add-on, the length of edges comprising the tree trunk were able to be computed on Edit Mode.

3D printing of complex mangrove structures

Based on the quality of the 3D mesh, three mangrove models scanned using the best method were chosen for 3D printing. We outsourced the 3D printing to a local vendor, which built the models using synthetic resin and coated them with non-toxic paint. These materials allow the models to physically resemble the actual trees as close as possible (Figure 6). Due to their large sizes, each model was printed in several separate components, which were stuck together before painting.

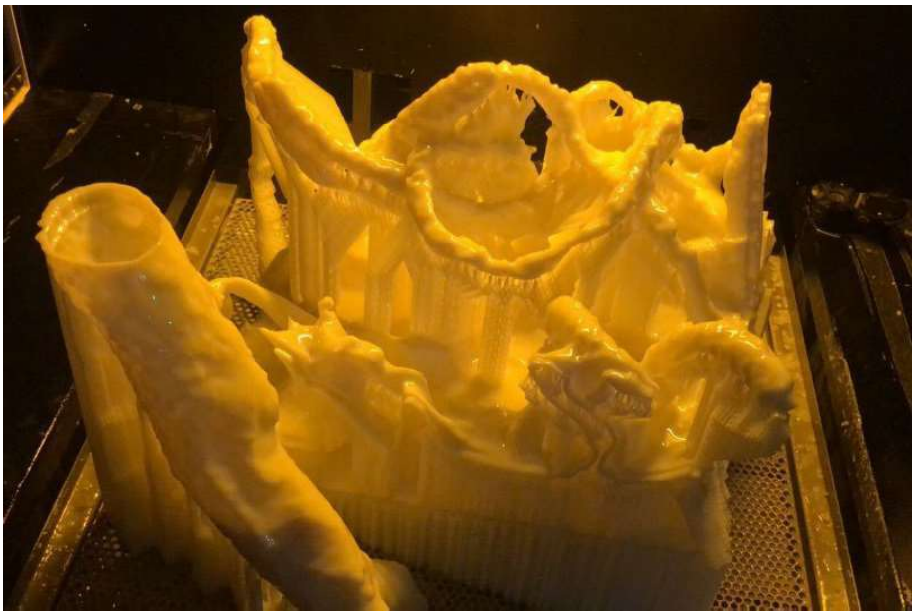

Figure 6. **3D printing process** of a mangrove tree model using synthetic resin. Due to its large size, the model was printed in several separate pieces and glued together.

Ex-situ predation experiments

The most abundant prey fish species (glass perchlet *Ambassis gymnocephalus* and mullet *Mugil cephalus*) found in WP1 were selected for use in the predation experiments. These fishes (total length = 3 to 5 cm) were regularly taken back to the laboratory to be used in predation experiments. As large predatory fishes were absent in our surveys, we resorted to purchasing sub-adult mangrove jack *Lutjanus argentimaculatus* (juveniles of this species were found in SH streams) around 25-30 cm in total length from a local fishery (n = 13). Prey fishes were separated by species and were kept in sheltered 130 L plastic tanks (57 × 79 × 43 cm), while predatory fishes were kept in two 7,000 L outdoor circular tanks (d = 300 cm, H = 100 cm). All holding tanks were supplied with constant flow-through seawater. All fish were fed according to their appropriate diet, e.g., *L. argentimaculatus* were given frozen shrimp every other day, while small prey fishes were fed with commercial fish pellets 2 × 5 days per week. Predatory fishes were starved for 24 hours prior to experiments to standardize hunger levels.

Predation experiments were conducted in outdoor circular mesocosms (d = 250 cm) using one mangrove model, two predatory fish, and fifteen prey fish of the same species. The mangrove model was placed in the centre of the tank, and the area surrounding the model was covered with sand to level the bottom. Water levels were adjusted to three different settings (25 cm, 40 cm, or 60 cm) to mimic different tidal scenarios observed in Hong Kong. Water

levels were adjusted prior to placement of any fish into the tank. Prey fishes were collected from their holding tank and allowed to acclimate in the experimental mesocosm for 1 hour prior to video recording. Four underwater video cameras used in WP1 were placed on the bottom of opposite sides of the tank to maximize coverage of observable areas in video recordings. We recorded fish behaviour for a total of 40 minutes: 20 minutes before the introduction of predatory fish and another 20 minutes after. Predatory fishes were immediately collected afterwards to stop predation events from further occurring, and the number of prey fish remaining was counted.

Videos were transferred to a desktop computer and combined into one file as four separate frames using OpenShot Video Editor v-2.5.1 (Figure 7). Fish behaviour, prey schooling type, prey swimming pattern, vertical positions, and horizontal positions were recorded at every 0 second of every minute (e.g., 0:00, 1:00, 2:00, and so on) (Table 4). However, exceptions were made if fish were not visible at a specific second, in which we would interpolate data from the nearest second before or after that point. The number of chases, attack attempts, and successful attacks were recorded from the entirety of each minute, allowing for the calculation of success rates from every predation experiment. In this analysis, chasing is defined as the moment when a predator accelerates in the direction of a prey; attacking is defined as the moment when a predator opens its mouth to engulf a prey; and an attack is deemed successful when an attack results in the reduction of total prey in the environment.

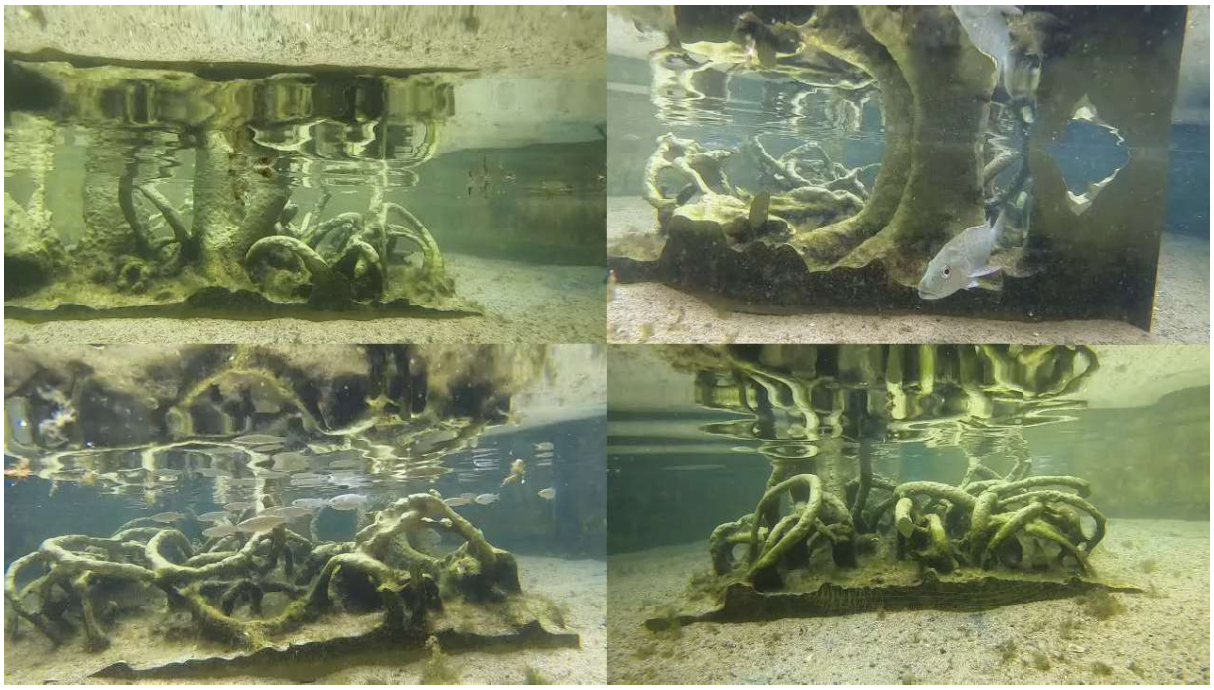

Figure 7. Combined video for data analyses.

Table 2. Fish behaviour recorded from video recordings.

Type	Species	Behaviour	Schooling pattern	Swimming direction	Mangrove use	Vertical position
Predator	*Lutjanus argentimaculatus*	Swimming Stopping	N/A	N/A	Inside Outside	Top Middle Bottom
Prey	*Ambassis gymnocephalus* *Mugil cephalus*	Grazing Swimming Stopping	One group Split groups Dispersed	One direction Zig-zag Haphazard	Inside Outside	Top Middle Bottom

Work Package 3 (WP3) Individual-based modelling of use of mangroves by juvenile fish

The purpose of this work package was to describe the pattern of juvenile fish use of mangrove patches by developing an individual-based model (IBM). The model would include all parameters that are known to influence choice of habitats by juvenile fish, such as salinity, water flow, and turbidity. This work package was conducted in collaboration with Dr Uwe Gruetters of Justus Liebig University Giessen, Germany.

The final model InMangrove was developed based on earlier work on a similar model InSTREAM. The work leading to the development of the IBM model is summarised below.

Working step 1: Translation of the InSTREAM model

Preview

InSTREAM purpose(s): The **in**dividual-based **S**tream **TR**out **E**nvironmental **A**ssessment **M**odel (InSTREAM) version 7.1 predicts the response of trout populations and communities comprising different trout species to abiotic (environmental) and biotic change in streams. This includes trout responses to alterations of stream flow by hydraulic engineering projects, such as dam construction. inSTREAM was utilized as the base model for the development of inMANGROVE, an individual-based model (IBM) to predict juvenile fish behaviour in response to environmental and biological changes that occur in mangrove habitats.

Entities and state variables: The model simulates hydraulic conditions in stream reaches with state variables including flow, temperature, turbidity, and density of piscivorous fish (larger trout among others).

The state of the smaller dimensioned cells is given by their x/y-coordinates, their area (minimum = 1 m^2), the light irradiance, the velocity and depth, both hydraulic conditions being derived from reach hydraulics by way of rating curves, both assumed to be homogeneous inside a cell. The available/total fraction of cell area that provides velocity shelter, available/total number of hiding places (mainly for adult trout) and the distance to escape represent additional state variables. The state of a cell is further defined by the available drift and search food concentration, the latter being replenished by a predefined benthic area at each time step.

Trout contain the state variables: species, sex, age, length, weight, condition (fraction, 0-1), maximum speed, activity (drift feeding, search feeding or hiding), inhabited cell, superindRep (number of juvenile fish contained in a super-individual), consumptionMemoryList (covering consumed items over all time steps of the same day), growthMemoryList (over 1.0 d at most), and survivalMemoryList (survival probabilities experienced during this day). Fish eggs represent a further entity as reproduction is likewise modelled in the IBM, but we shall not be reporting details of the eggs' state here.

Processes and scheduling: At each time step, the following updating actions were scheduled in consecutive order: (1) time update; (2) update of reaches and cells; (3) fishes' update; (4) eggs' update; and (5) output generation.

At the core of the fishes' update were the following actions: Fish select an activity among drift feeding, search feeding, and hiding behaviour on the basis of their life stage and size, local hydraulic and other environmental conditions. Additionally, fish take various mortality risks into account, among them the risk to become prey to terrestrial predators or piscivorous fish. They decide to move to the adjacent cell that is predicted to provide the best growing conditions at the lowest mortality risk. The fish then show the feeding behavior for which the cell provides the best fitness and grow accordingly. In principle, the decision-making is based on a trade-off between mortality and growth, estimated by a full bio-energetic sub-model. Movement distance, in turn, depends on the size of an individual fish. Overall, the decision for hiding or feeding depends on cell-specific attributes such as the fraction of cell area that provides velocity shelter, the number of hiding places, and the distance to escape. During the spawning season, trout reproduction completes the fish update.

Advancement of the IBM in recent years has focused on a refinement of the temporal scale (i.e., time intervals) by including the diurnal light phases (night, dawn, day, and dusk). This concludes our brief InSTREAM descriptive overview.

Assessment of the InSTREAM value: The model has played a key role in the development of IBM theory and served as one of the showcase models in the ground-breaking book "Individual-based Modeling and Ecology " (Grimm and Railsback 2005). It is a mature IBM that has been under continuous development by Steve Railsback and colleagues for more than 20 years (Railsback et al. 1999; Railsback et al. 2021) and has been ported to the agent-based modeling framework Netlogo (https://ccl.northwestern.edu/netlogo/) since 2016 (Ayllon et al. 2016, Railsback et al. 2021). With the attributes described above, it will likely provide a universal model for the simulation of mangrove usage by juvenile fish populations.

Feasibility of model adoption for juvenile mangrove usage: Since the procedural-like Netlogo program is merely available as a large uniform code base, it seemed hardly feasible for us to adapt the original model to this new application.

Thus, we considered it necessary to translate the model to MASON/Java in order to take full advantage of object-oriented programming (OOP) principles: we gained simplicity, flexibility and extensibility by decomposing the complex problem into smaller discrete and

decoupled components while benefitting from the rewards of standard design patterns (Gamma 1995). Usage of JUnit and Mockito testing capabilities in Java ensured correct translation; encapsulation made the code more secure; debugging facilities of the Integrated Java Development Environment Eclipse made the program easier to troubleshoot (Figure 8).

Actual model translation work

Translating the original model comprising 162 pages of code represented a great effort. An important design decision was therefore made at the beginning of this work. We used the log4j2 library and Java logging facilities therein to create various csv output files, whose contents and structure were made identical to those produced by the original model. This allowed for easy later comparison of model behaviour.

Direct translation of the Netlogo code and restructuring of the program while abiding by OOP principles as well as following general recommendations on how to design an IBM with MASON and introducing design patterns worked hand in hand. We chose a layered architecture for the model. In accordance with the MASON manual, we created an InMangroveModel class and a separate InMangroveModelWithUI class for model visualization. The code of all model entities detailed above was put in separate similarly-named classes (i.e., Reach, ACell, Fish, Eggs class). Several design patterns were introduced: ModelParameters were implemented as Singleton pattern, and FishSpeciesParameters as Multiton pattern. An Observer pattern regulated the decoupled data exchange between the InMangroveModel object and the Fish objects. We separated the structural objects, such as fish or cells, from their functionality by way of the Visitor pattern. This design decision raised flexibility and extensibility of functionality. Class names such as SelectCellVisitor, LifeProcessesVisitor and SpawnProcessVisitor are a reflection of this introduction. Moreover, a Strategy pattern seamlessly controlled the generation of output files. As shown in Figure 8, we also created a 2D display following the template. Figure 8 compare screenshots of the 2D displays of the two models.

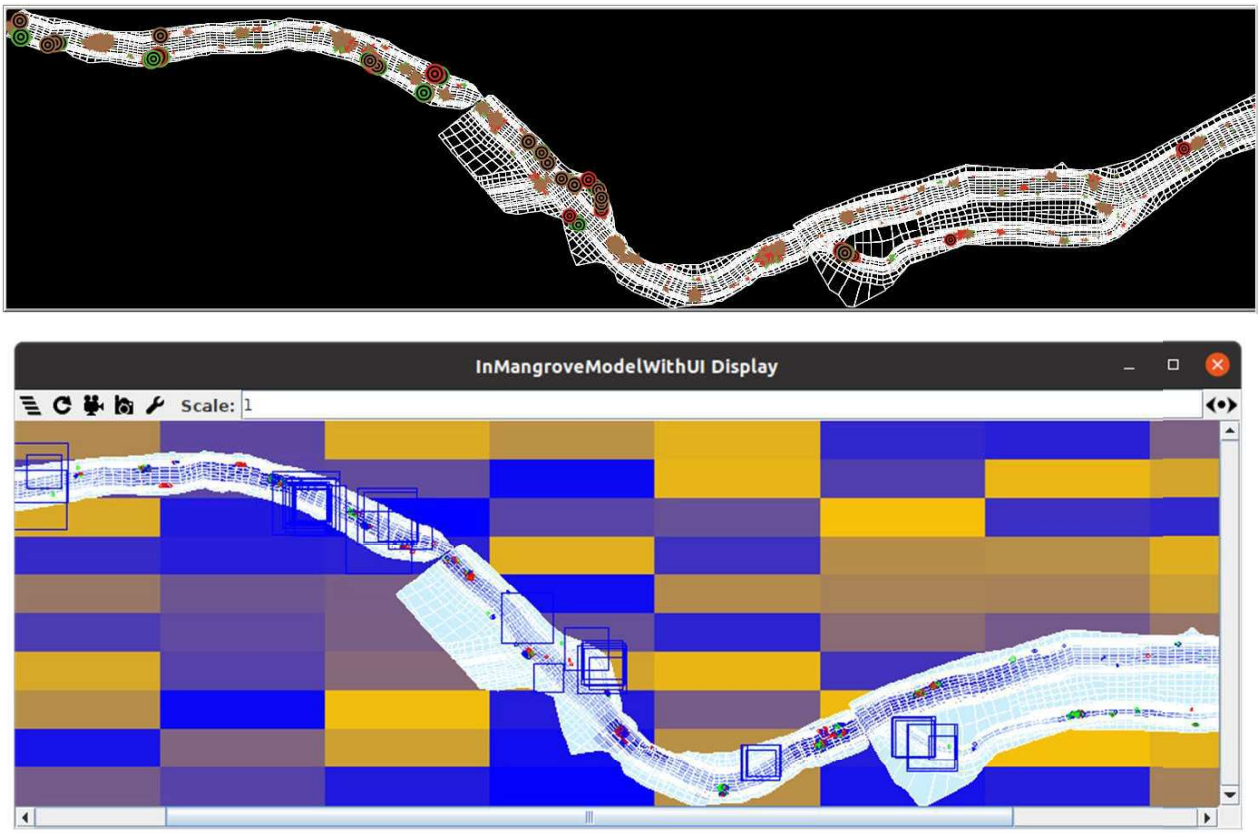

Figure 8. 2D-display of the Netlogo InSTREAM 7.1 model (top) and the translated Java version of InSTREAM 7.1 (bottom).

Working step 2: Evaluation of correct translation

The sophisticated strategy will be explained briefly using the testGrowthRateForWithHideSmallFish() method as example (compare Figure 9).
The method tests the calculateGrowthRateFor(..) method inside the SelectCellVisitor class with values that we obtained from a print-out of the same code in the original Netlogo model. calculateGrowthRateFor(..) makes method calls to the related Fish and Cell object.
In order to avoid the complicated need to create all involved objects, Mockito allows us, for instance, to create a simplistic mock fish object instead that can only return a value of ≈ 4.99 cm when the getLength() method of this "small-size" mock fish object is called. Likewise, the test method creates a spy of a SelectCellVisitor object that returns ≈ 62.34 when its calculateRespirationFor(..) method is called with the hiding behavior and an empty mock Cell object (a null object, to say).

In the end, a JUnit assertEquals(..) method call (not shown) tests whether calculateGrowthRateFor(..) of a true SelectCellVisitor involving the mocked/spied objects returns an identical value as the Netlogo code.

```
public void testCalculateGrowthRateForWithHideSmallFish(){
    Fish theFish = Mockito.mock(Fish.class);
Mockito.when(theFish.getLength()).thenReturn(4.995404838752025);
SelectCellVisitor scvSpy = Mockito.spy(selectCellVisitor);
Mockito.doReturn(62.340004776536674).when(scvSpy)
    .respirationFor(theCell, theFish, 0.0);
```

Figure 9. **Coding.** Part of the Junit/Mockito testCalculateGrowthRateForWithHideSmallFish() method (compare verbal explanation in the text)

Running all the written Junit and Mockito test classes combined in a TestSuite yielded successful results. Hence, tested calculations of the Java model are identical to those of InSTREAM.

Furthermore, we compared a single output file of each type produced by the Java model with that of a corresponding Netlogo output file using a customized Excel file. Since these output files contain thousands or more Excel cells that need to be compared, we used conditional formatting along with averaging pivot tables in Excel for fast visual detection/inspection of differences. Figure 10 shows two examples being part of this kind of Excel file.

End of time step	Light phas	Reach	Species	Age class	Count
2000_10_08_05_	night	Upstream	Rainbow	Age-0	73
2000_10_08_05_	night	Upstream	Rainbow	Age-1	1
2000_10_08_05_	night	Upstream	Rainbow	Age-2+	-2
2000_10_08_05_	night	Upstream	Brown	Age-0	-162

Average of FractionDriftFeeding			
Age-0	Age-1	Age-2+	
0.037931414	-0.01511104	-0.04223784	
0.025608634	-0.01020369	-0.00636983	
0.092782409	0.062996456	0.00080044	
0.035035063	**0.016019526**	**-0.01535744**	

Figure 10. **Example Excel output file (1)** that compares csv output files of single model runs. A pivot table is shown at the bottom.

For the comparison, we started the respective model run in Java and in Netlogo with the same random seed. The random seed determines the starting position in a long series of

random numbers contained in the random number generator (RNG). The seed affects the outcome of stochastic processes; model outcomes are identical if the same model is started twice with the same random seed.

However, even though MASON and Netlogo use the same RNG and both models were started with the same random seed, model outcomes were not identical, likely because Netlogo does not only call the RNG inside the model code, but also in the background. For example, to shuffle lists of entities randomly. Therefore, we could not be certain whether differences were systematic or due to randomness.

To overcome this issue, we adopted a third comparison strategy. We collected output files from 10 Java and 10 Netlogo model runs and conducted either statistical comparisons of means using a two-sample t-test when its assumptions (normality, homogeneity of variances, absence of outliers) were met or a non-parametric comparison of medians using a Wilcoxon-test, if otherwise. These tests were conducted with the R statistics software (R Development Core Team 2012) and were carried out for all values contained in the output files. Results were summarized in an Excel file, again using conditional formatting for rapid visual detection of statistically significant differences. Besides, the R-script automatically saved a Box-Whisker plot for each significant difference. Figure 11 shows an example being part of such a summary Excel file. Figure 12 depicts one of the Box-Whisker plots.

	End of time step	IsCensus?	Light phase	Reach	Flow	Temperature	Turbidity	Species	Age class	t,w Count	p-value Count	p-significance Count	Difference Count	Mean,Median of Java Count	Mean,Median of Netlogo Count	CI Low Count	CI High Count
30	2000_10_08_05_53_04	FALSE	night	Upstream	28.3625	8.3	2.83625	Rainbow	Age-0	2.265227	0.038	T-test: *	469.5	2192	1722.5	29.52249	909.4775
31	2000_10_08_05_53_04	FALSE	night	Upstream	28.3625	8.3	2.83625	Rainbow	Age-1	66	0.227	Wilcox-test: ns	1.00E+00	97	95.5	-0.99995	2.999965
32	2000_10_08_05_53_04	FALSE	night	Upstream	28.3625	8.3	2.83625	Rainbow	Age-2+	71	0.111	Wilcox-test: ns	1.000007	51.5	50.5	-1.2E-06	2.999994
33	2000_10_08_05_53_04	FALSE	night	Upstream	28.3625	8.3	2.83625	Brown	Age-0	62	0.393	Wilcox-test: ns	3.05E+01	395	363	-46	137

Figure 11. **Example Excel output file (2)** that summarizes results of statistical comparisons of means/medians. According to a t-test, the average count of rainbow trout in the Upstream reach at 5:53.01 a.m. of October 8 2010 was significantly different between the Java and Netlogo model runs.

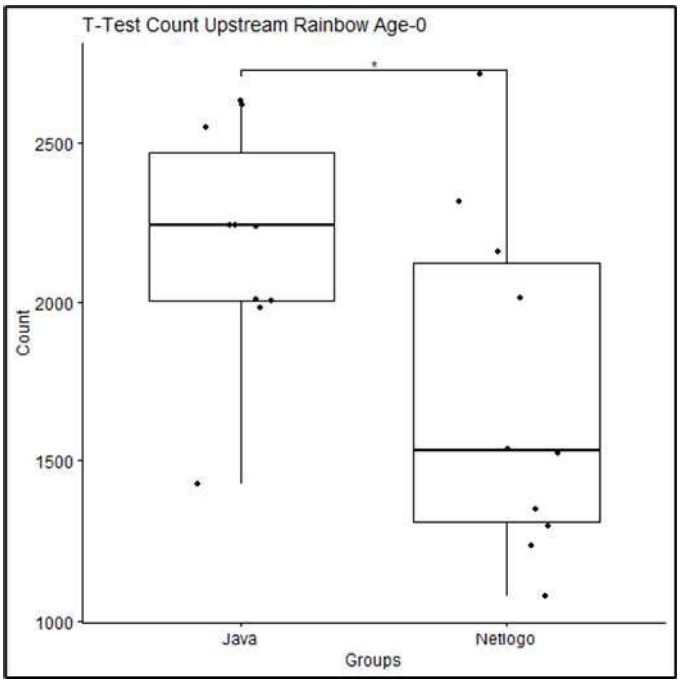

Figure 12. **Box-Whisker plot** corresponding to the t-test result presented in Figure 11

Since their completion, comparison files revealed that the two models exhibited systematically different behavior with apparent spatial patterns. Hence, we urgently searched for errors in our code using the Eclipse debugging facilities and found a range of them. However, despite all the implemented corrections, systematic differences persisted until the beginning of October. At that time, Senior Research Assistant Leon Metzger recognized a false behavior of a single fish in the original Netlogo model. This fish had selected search-feeding because this behavior provided the best fitness in an adjacent cell. However, due to a bug in the Netlogo code, the fish was "transported" to the best drift-feeding cell instead and enacted the search-feeding behaviour there. Obviously, this error deteriorated the activity and cell selection process. We further recognized that we had corrected this bug in our Java model a long time ago without double-checking the original model. In fact, after we had reintroduced the bug into our code, only a very low number of significant differences remained. Apparently, we had reached a breakthrough.

We immediately informed the InSTREAM model developer Steve Railsback about the bug and our finding is now specially mentioned and appreciated on the InSTREAM website at Humboldt State University, CA, USA.

We concluded this working step with long-term model runs spanning two years with both models. Figure 13 visually compares total fish abundances by age class of the two models. Obviously, all abundance fluctuations within the original were mirrored by our

translated model. We attributed the deviation in maximum fish abundances between the models as effects of stochasticity (see above). Thus, we interpreted the results as indication of correct translation.

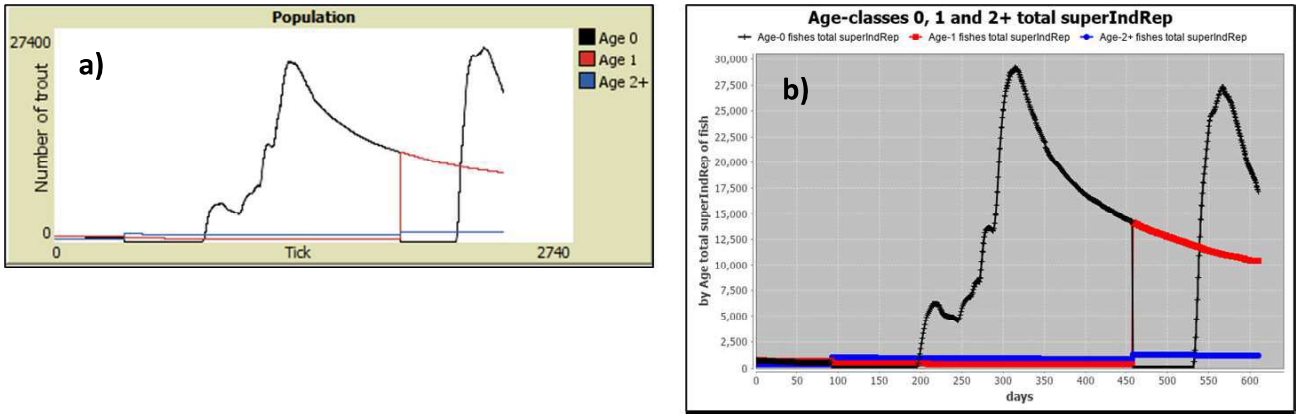

Figure 13. **Comparison of fish abundances by age class** between a) the original Netlogo model and b) our translated Java model

Working step 3: Choice of a site for the simulation study

At present, almost the entire coastline of the Pearl River Estuary is urbanized. Anthropogenic intervention has left only small-scale mangrove remnants scarcely interspersed along the coastline (Liu et al. 2008).

An exception to this bigger picture are the intertidal mangroves of the Mai Po Marshes Nature Reserve, Hong Kong, which comprise the sixth largest area of protected mangrove in China (Young 1999), and the Futian National Nature Reserve, Shenzhen, China. The mangroves of these nature reserves fringe the Deep Bay and are situated on both sides of the border between the New Territories of Hong Kong and the Shenzhen Special Economic Zone. The intertidal Mai Po mangrove area alone covers 319.3 ha (Jia et al. 2014). As the Mai Po Nature Reserve and Inner Deep Bay are recognized as a wetland of international importance under the Ramsar Convention, they have attracted a lot of interest by scientific researchers and, thus, a rich database regarding the mangrove area exists. Primarily because of the high data requirements of the IBM to be developed, we chose a site within the Mai Po Nature Reserve for this simulation study.

The InMANGROVE-IBM provides three parameters by which structural complexity of mangroves exerts a likely protective influence on juvenile fish. For their spatially-explicit parametrization, we are in need of a species-distribution map for the study site, since structural complexity varies in a species-specific way.

Fortunately, a number of articles have mapped the species distribution of mangrove forests in the Mai Po area, mostly on the basis of remote sensing (Cao et al. 2021, Jia et al. 2014, Jia et al. 2016, Li et al. 2020, Li et al. 2019, Liu et al. 2008, Liu et al. 2018). We chose the species distribution map that was derived by Li et al. (2019), because of its high spatial resolution (2m × 2m), the canopy height model included in the article and because other required data was also available for the site. Figure 14 shows a classified raster of the species distribution map created by us with the GGIS software. Figure 15 indicates the location of the site within the Pearl River Estuary Region.

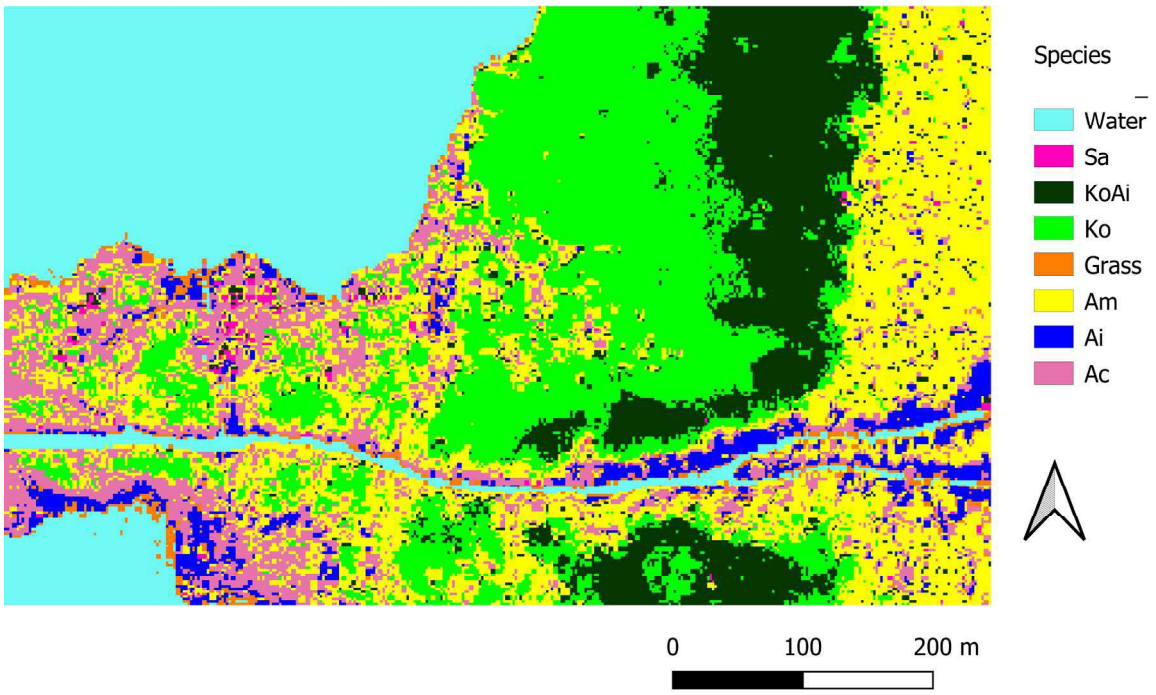

Figure 14. Classified species distribution at the Mai Po Nature Reserve, created from Li et al. (2019) using the QGIS-software. Species names: Sa = *Sonneratia apetala*, KoAi = *Kandelia obovata & Acanthus ilicifolius*, Ko = *Kandelia obovata*, Am = *Avicennia marina*, Ai = *Acanthus ilicifolius*, Ac = *Aegiceras corniculatum*

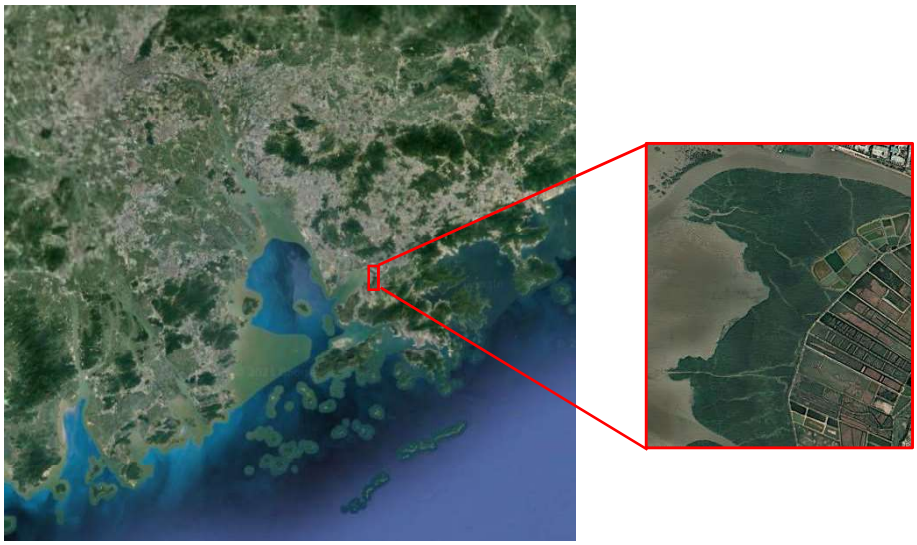

Figure 15. **Site location for the simulation study** within the Pearl River Estuary Region (from Google Earth)

Working step 4: Derivation of structural complexity for different mangrove species

The extent and type of structural complexity differs among mangrove species. It consists of a carpet of upright pencil-shaped pneumatophores in the case of *Avicennia marina* and *Sonneratia apetala*, a covering by near-ground spiralling prop roots in case of *Kandelia obovata*, a dense thicket of stems for *Acanthus ilicifolius* or multiple stems in case of the shrub-like *Aegiceras corniculatum*.

Since the likely protective influence of these structures is presumably also species-dependent, we needed to assess the extent of structural complexity around individual trees in a species-specific and spatially-explicit way. The strategy we chose to accomplish this task is illustrated in Figure 16 and verbally outlined below.

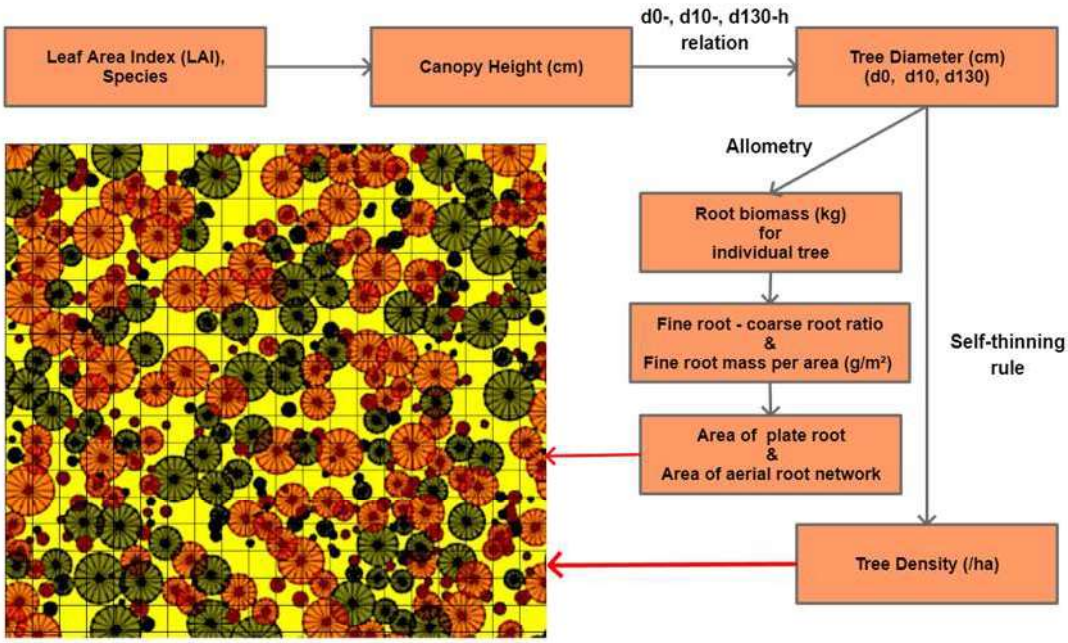

Figure 16. **Calculations for deriving aerial root system radii** and distribute root systems of individual trees on the site, as shown on the integrated image

It was our objective to assess either the radius of the (aerial) rooting system around an individual tree (for species: Ko, Am, Sa) or merely the tree density (for species: Ai, Ac). We intended to place the circular aerial rooting systems or trees of the estimated dimensions on the site –in accordance with the species distribution.

We began with the species distribution map of Li et al. (2019). The copied map was loaded into QGIS and geo-referenced using an aerial map of the region. Subsequently, the resulting map was classified with the Raster Calculator in QGIS, vectorized to polygons that surround species-specific regions and exported as ArcGIS shape file.

Since Li et al. (2019) provided species-specific canopy heights merely as Box-Whisker plots, but not as spatial Canopy Height Model (CHM), we had to develop a workaround to retrieve canopy height varying in space. Towards this end, we accessed Sentinel-2A satellite imagery of January 18, 2018, at the SciHub website (https://scihub.copernicus.eu/dhus/#/home) of the European Space Agency (ESA). The Biophysical Processor within ESA's Sentinel Navigation Platform (SNAP) was used to calculate the Leaf Area Index (LAI) of the Mai Po area at high resolution (10m × 10m). The raster map of the LAI (geotiff format) was then postprocessed in QGIS, aligned with the species distribution and clipped to the same extent. The LAI values were added to the

attribute table of the species distribution shape file and the shape file was successfully imported to the InMANGROVE model.

It was our aim to linearly interpolate species-specific canopy heights from the LAI values. We aligned each species-specific minimum/maximum canopy height reported by Li et al. 2019 to the minimum/maximum LAI on the map. Once canopy heights in space were known, local tree diameters could be obtained from general diameter – height relationships. We based the derivation of these relationships on diameter at ground level and tree height data collected by Duke and Khan (1999) (Tables 2, 4, 6, 8) along a transect located at the southern margin of our site in Figure 7. Following the approach of Botkin et al. (1972) and Shugart (1984), we fitted the following quadratic tree height equation to the data using the R statistics software:

$$H = b_3 \cdot D_h^2 + b_2 \cdot D_h + h \qquad (1)$$

where H denotes tree height (in cm), D_h is the tree diameter (cm) measured at height h (cm), b_3 is a parameter, b_2 is an auxiliary variable that can be calculated by $b_2 = \text{sqrt}(4\ a\ (h - h_{max}))$ with h_{max} being the maximum tree height (cm) and h is the intercept of the quadratic equation

We first fitted equation 1 to measured diameters at ground level D_0 for each species. In the fitting, the assumptions were made that the canopy heights reported by Li et al. (2019) represented the maxima for the involved species in the region. Thus, we forced the fit to have a maximum there. As most of the published allometric relationships for root biomass (= below-ground biomass) we strived for depend on D_{130} or D_{10}, we had to fit a height-diameter relationship for those as well. This was done under the assumption that the frequently observed linear conversion between D_0 and D_{130} holds and that the quadratic parameter b_3 remains the same (justified by Figure A2, Appendix A, Grueters et al. 2021). In principle, we minimized the sum of squared deviations between the H-D_0- and H-D_{130} relationships using constrained optimization with the optim function in R and fitted solely the linear D_0 D_{130} conversion parameters. Figure 17 shows both fits using *Avicennia marina* as example.

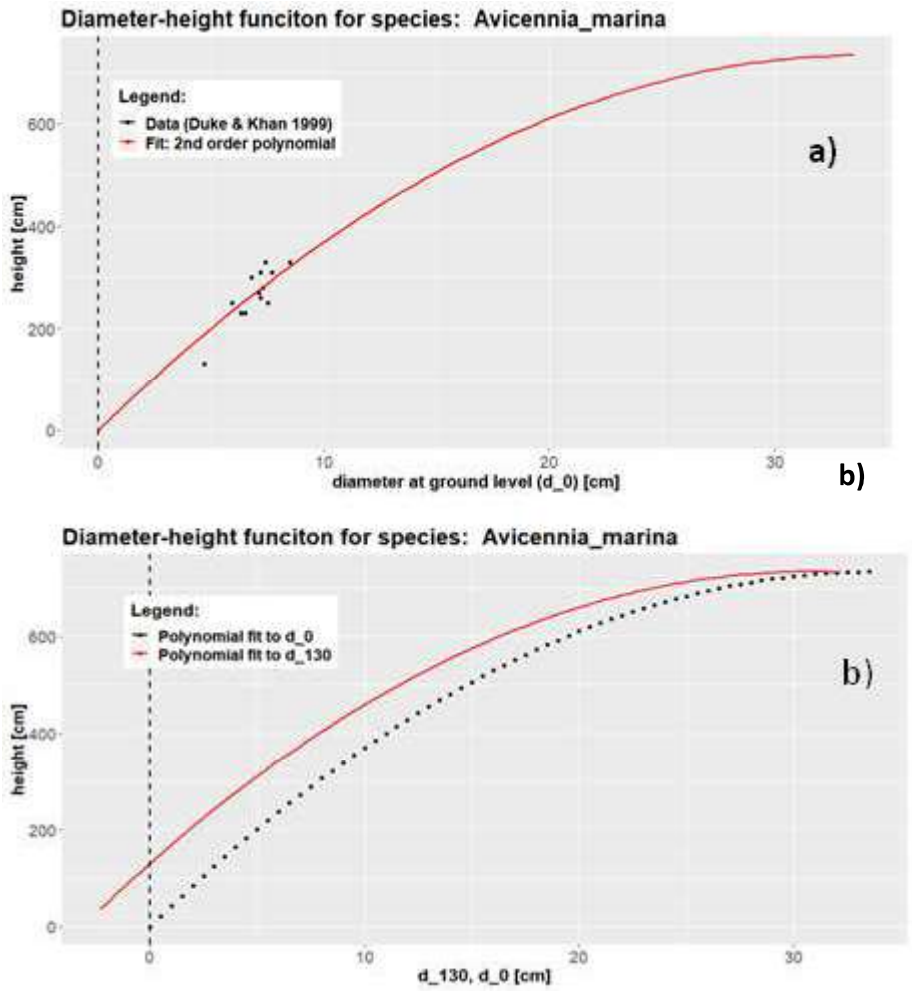

Figure 17. **Diameter - height relationships.** a) Height - D_0; and b) Height - D_{130} relationships

Root mass - (diameter × height) allometric relationships were taken from the literature (*Kandelia obovata*: Hoque et al. 2011, *Avicennia marina*: Wang et al. 2014, *Sonneratia apetala*: Zhu et al. 2011). We paid particular attention to include allometric relationships from sites as local as possible. We used the fine root mass per area (in g m^{-2}) measured by Zhang et al. (2021) as parameter. However, the fraction of fine roots in total roots that mediates between the previous two parameters has rarely been measured. Thus, we had to fall back on to Castaneda-Moya et al. (2011) who have examined the parameter in the Neotropics. We were then in the position to calculate the radius of root systems for individual trees, but in order to distribute root systems on the site, the tree density was still needed.

In general, there exists an allometric relationship, called the self-thinning line, between tree diameter and tree density per hectare (Reineke 1933, Pretzsch and Biber 2005). In the last two decades, Stochastic Frontier Analysis (SFA) has proven to be an effective

technique to derive and explore the self-thinning boundary line of trees (Bi 2004, Weiskittel et al. 2009, Bogetoft and Otto 2011), particularly because SFA allows for flexible model construction including covariates and useful statistical model comparison via likelihood ratio tests. Following the example of Weiskittel et al. (2009) we fitted the following self-thinning boundary line to the single-species data of Duke and Khan (1999):

$$\ln(N) = \beta_0 + \beta_1 \ln(D_0) + \beta_2 \ln(PBA) \qquad (3)$$

where N denotes tree density per ha, D_0 refers to the diameter at ground level [cm], PBA is the partial basal area of a species and β_0 represents the intercept in an ln-ln-plot.

We also attempted to construct models with additional species-specific slopes and/or intercepts, but none of these models had a significantly better goodness of fit than the model presented in equation 3. The analysis was carried out with the sfaR library in the R statistics software. The self-thinning slope was estimated to be at -1.982 and the intercept amounted to 12.775. Both represent reasonable values. Figure 18 illustrates the fitted self-thinning boundary line. All calculated parameters were inserted into the properties file and were ready to be used in the model. Working step 4 was then completed. At the end, it is emphasized again: the derivation of the self-thinning line is the only requirement to address the structural complexity of species that lack aerial root networks.

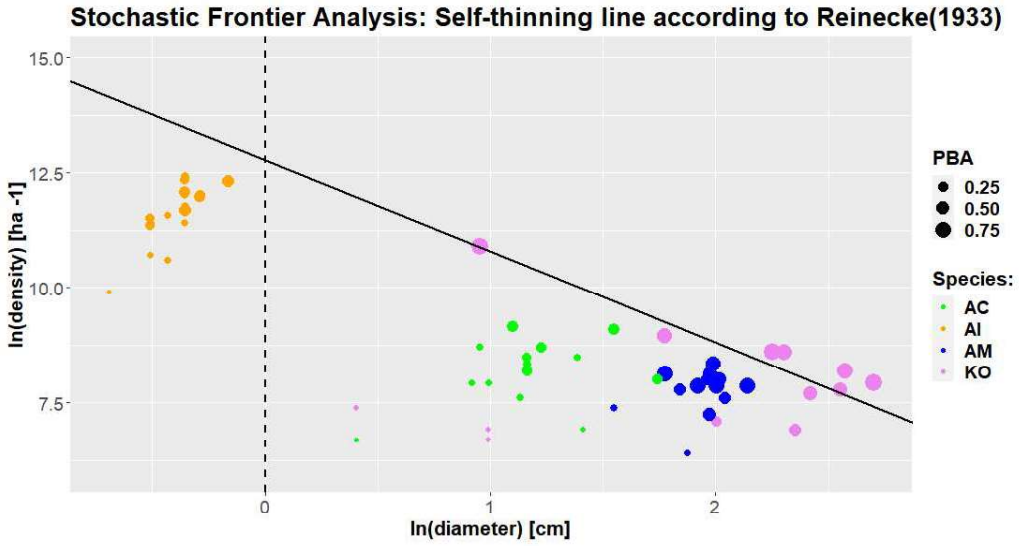

Figure 18. **The self-thinning boundary line**, calculated for the mangrove species Ko, Am, Ac, Ai, including PBA = partial basal area

Working step 5: Derivation of the light intensity below the canopy

It has been recurrently found that shade played an important role in the habitat preference of juvenile fish (Nagelkerken et al. 2008). Thus, mangrove LAI data is also beneficial, because it allows for the simulation of the light attenuation by the canopy. Usually the light intensity (I) below the leaf area index (F) is calculated using the Lambert-Beer equation (Monsi and Saeki 1953):

$$I = I_0 \cdot e^{-K \cdot F}$$

where I_0 refers to the incoming light intensity (above canopy) and *K* denotes the canopy light extinction coefficient.

Since the canopy light extinction coefficient *K* was available for Chinese mangrove forests with almost equal species composition (Guo et al. 2021), we were able to attenuate the cell light based on the leaf area index.

Working step 6: Harmonic tidal prediction and tidal scheduling

In the chosen mangrove site, tides set the pace to the life of juvenile fish. Even the extended mudflats directly offshore to the mangroves tend to fall dry during certain low tides (spring tide), leaving the tidal creek/channel on the site to be the only submerged refuge. This suggests that juvenile fish have to commute considerably.

Therefore, we considered it absolutely necessary to implement a TidalManager class and integrate it with the present SolarManager. A prerequisite for this task was that we were able to predict harmonic tides parametrized from data of the nearby tidal gauge station Tsim Bei Tsui. We analyzed the station's high and low tides of the year 2021 with the Tideharmonics library in R and retrieved the amplitude and phase lag parameters for the seven major tidal constituents (semi-diurnal: M2, S2, N2, K2; diurnal: K1, O1, P1) along with the mean sea level and the origin (reference date time). Constituent parameters were added to the model parameters.

With guidance from Kowalik and Luick (2019), Tideharmonics code for Doodson numbers, longitudinal formulae, amplitude factor, phase factor and equilibrium harmonics of constituents were reimplemented in the TidalConstituent class. The TidalAndSolarManager, in turn, calculated the current sea level by iterating over all the constituents and adding their harmonic oscillation values to the mean sea level.

Scheduling was performed by the TideSearcher class with the help of a Brent optimizer. At model initialization, the TideSearcher determined whether the next tide was a

low or a high tide. If it was, for instance, a high tide the TideSearcher initializes itself in the tidal section “RisingTide I” and set a regulating multiplicator to -1 (Since the Brent optimizer can only find minima, function values are multiplied by -1 for the search of a maximum). The Brent Optimizer searched for an optimum within the next two hours. As long as it found the optimum at 2 hours, it had not found the next high tide and proceeds with the next tidal section, i.e., “RisingTide II”. If, on the other hand, the optimizer retrieved an optimum inside the interval of 0 - 2 hours, it had found the next high tide and switched and moved on to section “FallingTide I”. In case a light phase change occurred in between, the tidal section was kept and only the light phase altered. Because the interval to the next tide might vary between 2.5 and 10.5 hours, we kept Rising- and FallingTide I – VI in stock.

In the end, a Junit class was written, which tested successfully that Java code and Tideharmonics, gaining identical sea levels over a three-monthly time period at hourly intervals. Sea levels computed by Java were also printed to the console and a plot of this data was then generated in R. Figure 19 shows the respective plot.

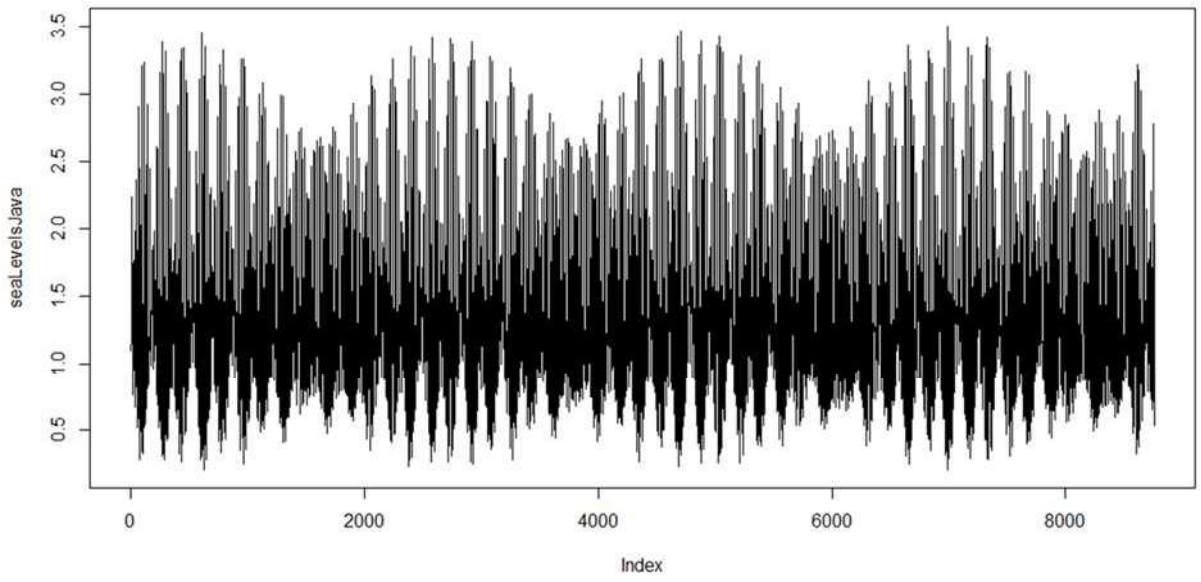

Figure 19. **Harmonic tide prediction and sea levels** calculated by Java code

Working step 7: Derivation of hydraulic rating curves

The InMANGROVE model has high requirements regarding hydrodynamic input data. Cell depths and cell velocities are important factors that influence fish behaviour in the model. Those were associated with reach flow in the InSTREAM model and have to be

associated here with tidal stages at the seaward boundary. These so-called rating curves, in turn, have to be derived from data generated by a hydrodynamic model.

For Deep Bay (DB), basically, two 3D hydrodynamic models have been calibrated. One was a Delft3D-FLOW model that simulates 3D hydrodynamics, sediment transport and salinities in the DB. Towards this end, it was combined with the larger-scale Pearl River Estuary Model (also Delft3D) to simulate sediment exchange at the "oceanic" stage boundary and SOBEK-1D to simulate sediment discharge into the bay by tidal rivers and drainage channels (Wang et al., 2011).

The other model was developed with the Environmental Fluid Dynamic Code (EFDC) and covers the entire Pearl River Estuary as simulation domain with grid refinement to 100 m – 300 m in the DB (Yang and Chui, 2017). Similar to the previous model, the EFDC-type model simulates 3D hydraulics, sediment transport and salinities in DB. In recent years, it has been applied to assess implications of Pearl River flow, land-reclamation, and sea-level rise for the Deep Bay (Yang and Chui, 2017, Yang et al., 2018, Yang and Chui, 2021).

Unfortunately, neither of the two models was able to simulate the hydrodynamics in the tidal channel and the mangrove area at our site, because of limited spatial resolution and lack of coverage. Therefore, we used the capabilities of the Hydrologic Engineering Center – River Analysis System (HEC-RAS, Brunner, 2021) instead to model hydrodynamics of the tidal channel.

The user-friendly HEC-RAS software has found wide usage worldwide (2,787 publications related to HEC-RAS, according to www.researchgate.net) and has been applied also in coastal to inland transition zones (Muñoz et al. 2021) and to mangrove creeks (Marois and Mitsch, 2017).

We applied the landscape engineering facilities in the software's RAS-Mapper. Research revealed that the tidal creek in question was rather a drainage channel of anthropogenic origin, constructed for the purpose to flush juvenile shrimps and fish through sluice gates during high tides > 2.4 m into the gei wai ponds that were located landwards of the mangroves. According to several literature sources (Cha et al., 1997, Young, 1999), the tidal creeks were desilted/dredged at regular intervals (10 years) and, based on the literature, we initially assumed that the creek could be treated as open channel of trapezoidal shape with 1 m depth (consistent with information that channel depth varies between 1.0 and 1.5 m

contained in various literature sources), 10 m top and 8 m bottom width. The engineering of the terrain was based on elevation data measured by Duke and Khan (1999) at 20 levelling sites between the bund wall and the mudflat at the mangrove fringe (500 m apart from the bund wall). Unfortunately, Duke and Khan used the mangrove fringe as datum and set its height, arbitrarily, to 0.00 m. Hence, it was necessary to correct elevations in relation to the mean sea level.

Relating the terrain to the mean sea level: Luo et al. (2020) estimated sediment elevation to be at 0.67 m above mean sea level on the mudflat at the mangrove fringe (their GW 3) and at 0.92 m about 100 m seaward of the bund wall to the gei wais (their GW 1). These estimates were made in 2018 for sites along and adjacent to a tidal creek that is situated in the proximity to the north of the transect measured by Duke & Khan (1999). Duke & Khan had measured an elevation of 0.52 m at their levelling site 4 100 m seaward of the bund wall. Thus, we made the decision to shift the entire engineered terrain by [0.67 + (0.92 – 0.52)]/2 = 0.54 m upwards. Figure 20 compares the original with the corrected elevation.

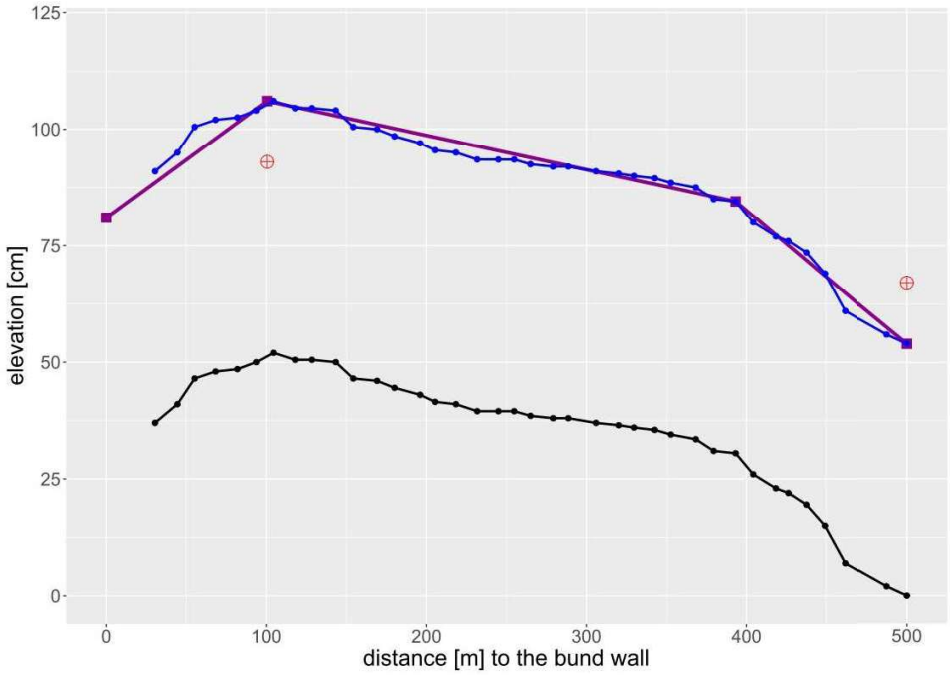

Figure 20. Terrain modification: Original elevation measured by Duke and Khan (1999) (**black**), Elevations estimated by Luo et al. (2020) (**red**), Corrected Elevation in relation to the mean sea level (**blue**), Simplified Elevation used by control points in RAS-Mapper (**magenta**)

We created a plane landscape of 0.54 m height with HEC-RAS-Mapper. Next, we raised the plane by a series of control points with heights marked by diamond symbols in the "Simplified Elevation" line of Fig. 13 and at respective distances from the bund wall. An open channel with the dimension detailed above was then virtually dredged.

Relating the tides to the mean sea level: The harmonic tide of the Tsim Bei Tsui tidal gauge station being related to the chart datum had to be corrected by subtracting the mean sea level of 1.442 m. Overall, this meant that we had to shift sediment elevation considerably up and water levels dramatically down.

Setting up the HEC-RAS hydrodynamic simulations with the modifications: We initialized HEC-RAS unsteady flow simulations with the modified tidal stage hydrograph as boundary condition at the seaward end of the area (see Figure 21) and – for the sake of simplicity – initialized it with a normal depth boundary condition at the bund wall. The latter was set up using a local friction slope measured over a distance of 100 m from the bund wall (0.0125 m/m). The first hydraulic simulation covered a period of 48 hours near a spring tide. The Manning roughness coefficient of the tidal channel(s) was estimated to be at 0.032 s $m^{-1/3}$ following the guideline of Arcement and Schneider (1989). A Manning's n of 0.02 s $m^{-1/3}$ was chosen for the open water (the mouth of the Shenzhen River and the mudflat). Because only water-depth dependent Chezy factors were available for Mai Po mangroves (Chan et al. 2011), we assumed that the Mai Po mangrove areas possessed a Manning's n value of 0.14 s $m^{-1/3}$. Hence, we applied the same value that was calibrated by Marois and Mitsch (2017) for a Neotropical mangrove forest.

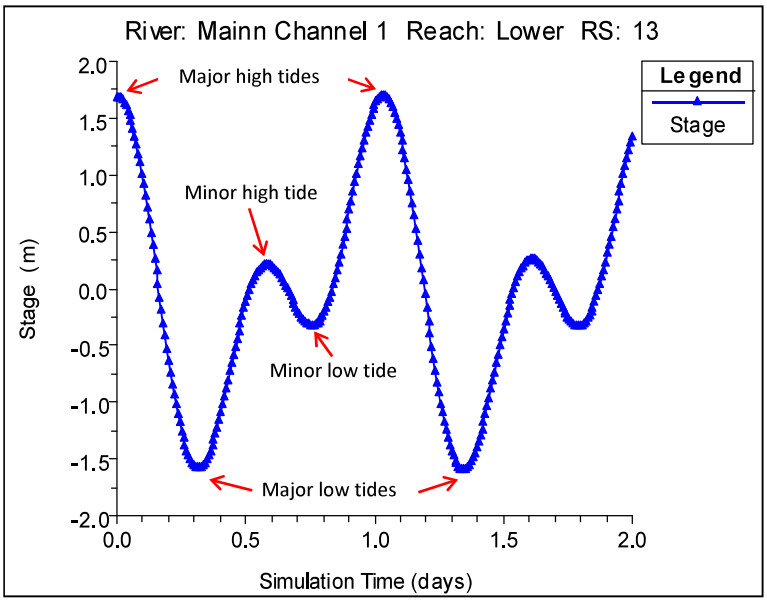

Figure 21. Stage hydrograph with major and minor tides of the mixed semidiurnal tidal regime at Tsim Bei Tsui. Boundary condition at the seaward margin of the study area.

Overcoming instabilities of the unsteady flow model: However, the consequence of the modifications was that the HEC-RAS hydrodynamic model went unstable and crashed early on. We implemented a number of strategies recommended by the HEC-RAS User's Manual and various forum contributions to overcome the detected water volume accounting error (between 18 and 22 % left the area unaccounted for) and to stabilize the model. The chosen strategies encompassed: (1) declining computational time step to 2 seconds; (2) reducing the grid size of the 2D mesh to 2 m x 2m; and (3) introducing a "pilot channel" of 30 cm width and depth of 2 m to keep at least a tiny amount of water in the tidal channel. We had to redraw the terrain repeatedly to remove steep parts of the area – a sort of terrain simplification (compare Fig. 12). In addition, we introduced break lines to align the mesh with local changes in terrain slope.

One or more of these strategies enabled the model to run to completion and, thus, we were able to visually inspect it for the first time. We realized a strange, so far un-described behaviour at the seaward boundary condition line when the tidal stage went below the minimum channel depth (-0.46 m): Semi-circular "holes" of water-free bare ground formed repeatedly and suddenly along the boundary line. These "holes" then refilled with water from landward cells over five to ten time steps. This led us to extend the area of interest by 500 m

into the mudflat to include part of the deeper bay (the bed of the Shenzhen River mouth) at the boundary. We assumed an elevation of –2 m (a water depth of 1 – 3 m was reported) at the boundary. By this means, there is still about 40 cm deep water left inside the boundary during the lowest (almost spring) ebb tide.

This represented a breakthrough: the unsteady flow model went immediately stable. We could bring the mesh size back to reasonable 10 m x 10 m, raise the time step back to 10 seconds, use the full mass and full momentum conservation equations in two dimensions, i.e., the St. Venant equation, apply the finite volume solver with mixed flow (accounting for sub- and super-critical flow) including Coriolis effects and water turbulence effects – in essence all settings recommended for highly fluctuating tidal systems in the HEC-RAS manuals.

Preliminary results of the unsteady flow simulations: Figure 22 shows the final engineered terrain.

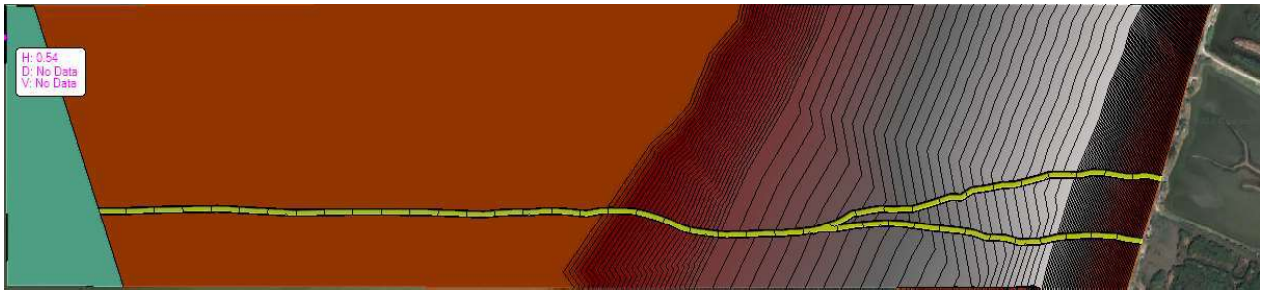

Figure 22. Terrain of the simulation area within the Mai Po Nature Reserve, engineered with HEC-RAS Mapper. Included structures: mouth of the Shenzhen River (green, on the left), mudflat of the Inner Deep Bay (uniform brown, to the left of the centre), mangrove area (brown to grey transition with contour lines, to the right of the centre), tidal channel (yellow), gei wais with bund wall (satellite image, on the right)

Figure 23 depicts the set-up mesh of the 2D flow area with a refinement region inside the tidal channel and break lines along sudden local changes in slope, among others: along the shoreline and the high ground 100 m seaward of the bund wall.

Figure 23. Mesh of the 2D Flow Area. The geometry was created with HEC-RAS Mapper. The tidal channel is shown almost in black as a consequence of the high-resolution refinement region (2 m x 2 m grid size) that was chosen to represent the more complex channel hydrology.

Figure 24 shows part of the refinement region inside the tidal channel and the break line located along the centre line of the channel.

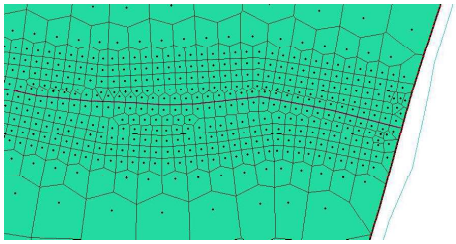

Figure 24. Part of the inner-channel refinement region (2 m x 2m grid size) near the gei wai bund wall (to the right)

The following set of figures illustrates the timelapse of a simulated falling tide in the studied area (Figure 25). It covers a period between the major high tide and the major low tide of the mixed semi-diurnal tidal regime at Tsim Bei Tsui.

Figure 25: Timelapse of a simulated falling tide

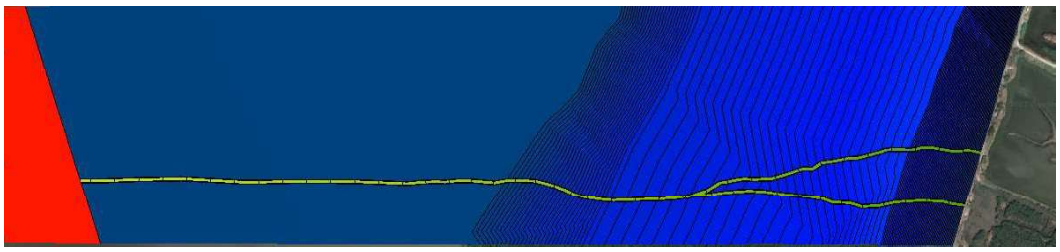

Figure 25a. Major high tide: Hydraulic simulation at a tidal stage of 1.685 m above mean sea level

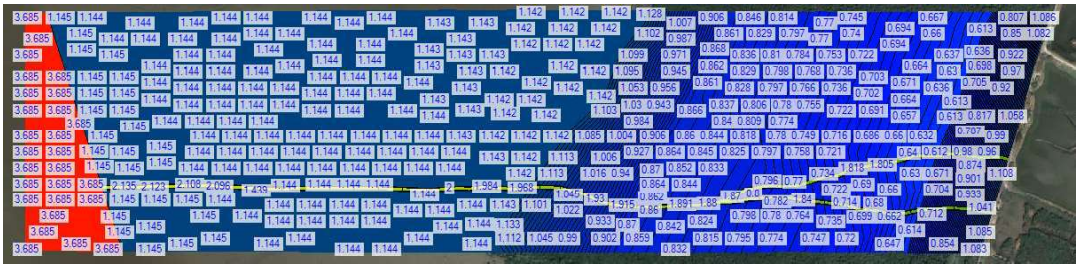

Figure 25b. Water depths [m] at the tidal stage of Fig. 18a.

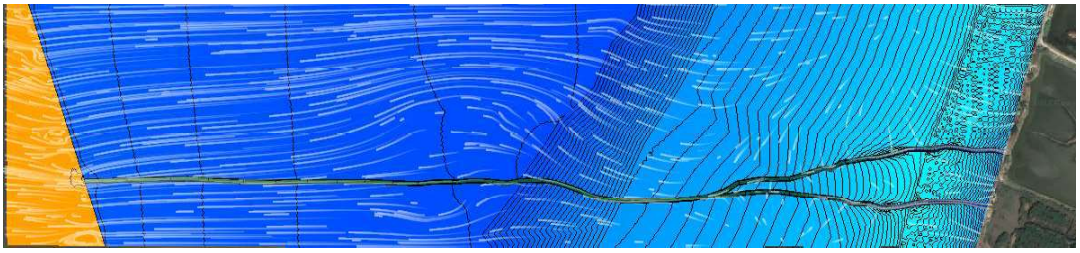

Figure 25c. Particle tracing to visualize the direction and velocity of the water flow at the transition between high tide and low tide. Water flows from the elevation peak located at about 100 m seaward of the bund wall in land- and seaward direction. The water in the tidal channels flows in a similar manner, but with much higher velocity (likely due to the lower Manning's n inside the channel). At several locations eddies of turbulent water have formed.

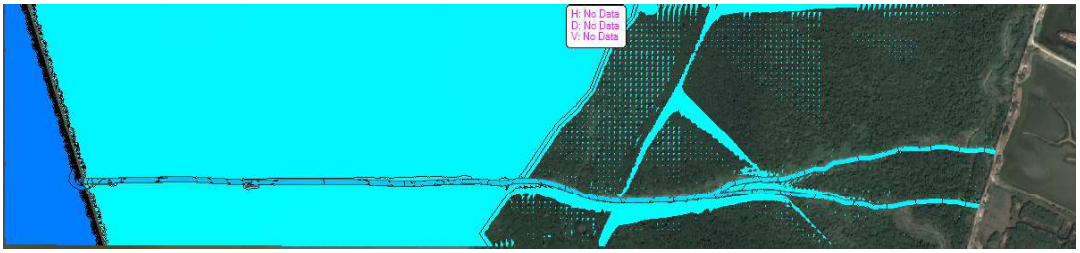

Figure 25d. Major low tide: Hydraulic simulation at a tidal stage of 1.604 m below mean sea level

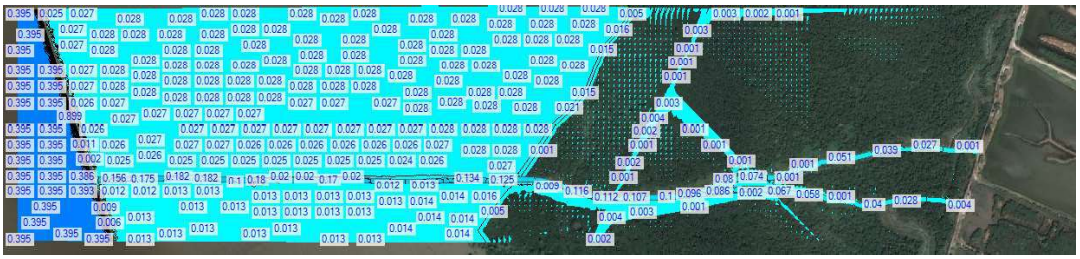

Figure 25e. Water depths [m] at the tidal stage depicted in Fig. 18d.

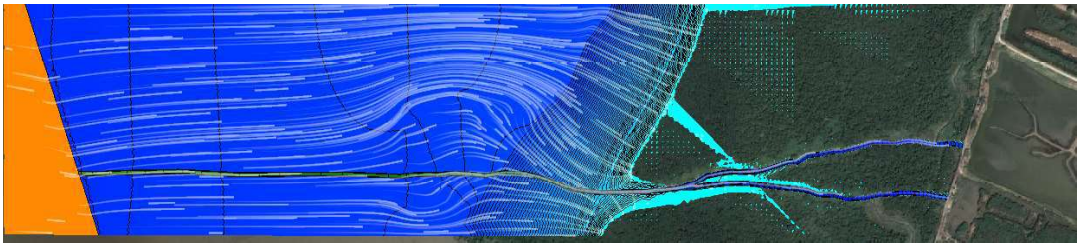

Figure 25f. Particle tracing to visualize the landward direction of the water flow at the transition between low tide and high tide. The water in the tidal channels flows also in landward direction, but with much higher velocity. Eddies of turbulent water have formed in the surrounding of the tidal channel seaward of the rising mangrove area.

Tentative conclusion drawn from low tide hydraulics: At a major low tide (near the spring tide), the entire mudflat and mangrove area have water depths equal to or less than 2.8 cm (0.028 m, compare Fig. 18d); water depths at the seaward end of the tidal channel amount to 18.2 cm at most and the depth declines gradually towards the gei wai bund wall. Because the elevation of the main channel's ground ranging between -46 cm and -8 cm is way above the tidal stage (-1.605 m), the presence of water in the channel is likely caused by the slow drainage of water from the mangrove area (due to their high Manning's n). Merely the water depth of 39.5 cm inside the mouth of the Shenzhen River is related to the tidal stage.

In the extreme case, when juvenile fish tend to escape to the bed of the Shenzhen River mouth during low tide, migration/commuting distance between the riverbed and the headland of the mangrove area around the mouth of the tidal channel would amount to 2 x 500 m and that between the riverbed and mangrove areas at the bund wall to 2 x 1,800 m per day. Given the small body lengths of juvenile fish in the Mai Po mangroves (2 – 16 cm), these migration distances appear substantial.

Therefore, we tentatively conclude that the likely long migration distances between places of refuge from ebb tides and feeding grounds in the mangroves might limit the potential of the Mai Po Nature Reserve as nursery habitat for fish species.

However, the following caution notes should be made about these conclusions:

(1) the conclusions shall be verified by field surveys made during low tides/spring tides.
(2) the engineered terrain shall be replaced by a digital elevation model derived from aerial imagery conducted with a LiDAR instrument. Please note that small-scale mangrove ponds might provide alternative places for fish to persist during ebb tides. For instance, Gedan et al. (2017) investigated mangrove ponds in Belize and Panama and found them to exhibit high abundance of macroalgae, macroinvertebrates, and fish.
(3) the hydrodynamic model shall be advanced through replacement of harmonic ties by tides simulated with a Deep Bay hydraulic model; replacement of the simplified open channel shape by surveyed channel bathymetry; and replacement of the normal depth boundary condition at the bund wall by a measured flow hydrograph at the sluice gate to the gei wai.

    Moreover, addition of the flow hydrograph might facilitate an intermediary rise in the channels' water depth. The hydrograph introduces the water discharge from the gei wai ponds during falling tides. This discharge is not accounted for yet in the HEC-RAS model. Discharge terminates when the water level in the Gei wai has dropped to the upper board of the sluice gate at 2.4 m above chart datum or 0.96 m above mean sea level after conversion. The HEC-RAS model should then be rerun with the flow hydrograph after a high ground at the bund wall has been added to the geometry. Likewise, a depression at the sluice gate and a storage area framing the perimeter of the Gei wais should be added to the modified geometry.

Deeper channel excavation during regular maintenance dredging and retardation of the gei wai discharge until low tide might encompass conceivable solutions to raise the channels' water depth during low tide and to reduce migration distances for fish.

Derivation of rating curves relating cell depths/velocities to tidal stage: Despite these considerations, we continued to work on our goal: the derivation of rating curves. Presumably, the required relationships in the mangrove area are more complex than those present in streams where high flows entering a stream reach are commonly associated with higher cell depths and velocities. Steve Railsback provided rating curves within the model input files of the InSTREAM model but did not explain in sufficient details on how they were derived.

Here, the task was accomplished by manually editing the RAS-Mapper initialization file to export raster files (in tif format) of the calculated/simulated cell depths and velocities at hourly timesteps over a period of 2 days (at first). Additionally, an ESRI shape file with the cell polygons and their attributes was exported.

Processing this data was conducted with the R statistics software (R Development Core Team, 2012). Initial inspection of scatter plots revealed that the relationship between the explanatory variable “tidal stage” at the boundary condition line and dependent variables, either cell depths or cell velocities, differed between major/minor tides and between rising/falling tides.

Notably, these relationships were affected by a combination of factors, such as the distance between a certain cell and the seaward/landward boundary condition line during rising/falling tide, the terrain details between them and the delay of the water conveyance to the cell, to name a few. The relationship was therefore unique for each of the approximately 20,000 cells. Fitting all these diverse relationships with parametric functions was thus not feasible. Instead, the non-parametric technique of LOESS regression (LOESS = Locally Estimated Scatterplot Smoothing) was used here.

A stepwise strategy was applied to select the “span” parameter that determines LOESS smoothing behaviour. First, a general-purpose optimization with the simulated annealing (SANN) method of the optim function in R was applied to determine cell-specific spans, each with the lowest sum of squared errors. This was done with error messages turned off. Then, a common span slightly above the found maximum was chosen and raised further in case errors occurred. As a last step, a judgement was made by visually inspecting LOESS regression plots that were created for 1 out of 200 randomly chosen cells. Figure 26 depicts a few examples of the created plots of both, cell depth and cell velocity rating curves.

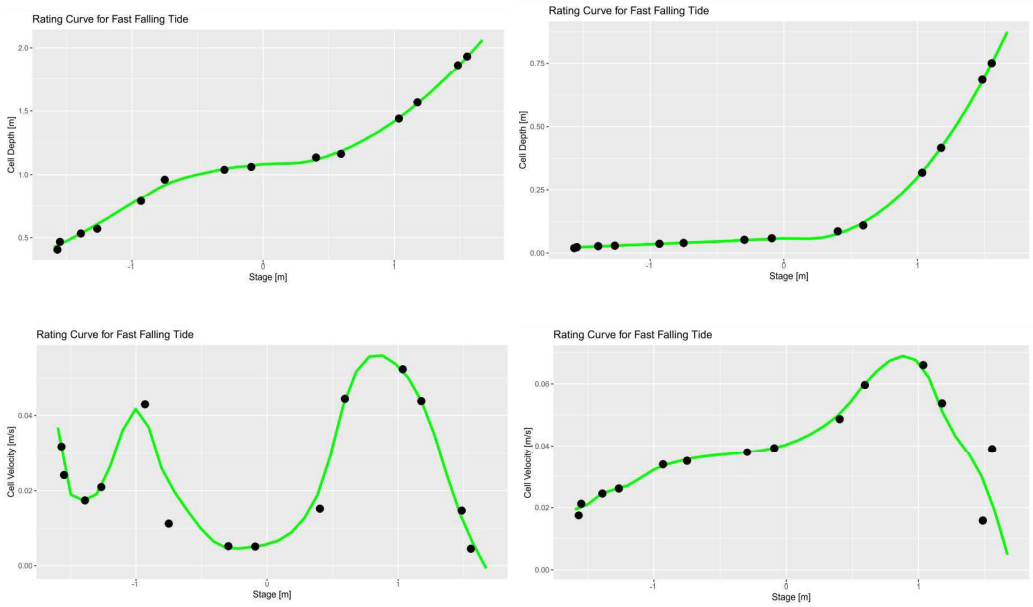

Figure 26. Exemplary depth, velocity rating curves during major falling tides.
Top left: depth vs. stage rating curve for the cell with ID 6847 (presumably: channel)
Top right: depths vs. stage rating curve for the cell with ID 9003 (presumably: mangrove)
Bottom left: velocity vs. stage rating curve for the cell with ID 12117 (presumably: channel)
Bottom right: velocity vs. stage rating curve for the cell with ID 9138 (presumably: mangrove)

The LOESS prediction function allowed us to calculate cell depth/velocity values for 33 equally-spaced tidal stages between the annual minimum (-1.604 m) and the maximum stage (1.685 m). Values of each rating curve were combined with the cell elevation and x/y-coordinates of the cell's centroid. Csv-files of the 20,000 cell-specific rating curves were collectively created for rising/falling tides and major/minor tides. These were then ready for usage as InMANGROVE model input. The coordinate/elevation information contained therein would enable us to select the fraction of cells to be simulated with the IBM. The area to be simulated was about half the size of that underlying the HEC-RAS model.

Working step 8: Potential solution to model calibration issues

Ideally, the individual-based InMANGROVE model should be calibrated using fish abundance data for different species measured in the field. However, it was hardly possible to achieve this due to the high protection status of the Mai Po Nature Reserve. We propose here a potential solution to this issue that involves the gei wai.

The gei wai intertidal ponds, constructed by Chinese immigrants in the 1940s, are considered to be an extensive form of shrimp/fish farming and sustainable usage of intertidal wetlands (Cha et al. 1997, Young 1999). Once shrimp larvae and juvenile fish have entered the pond, they feed on detritus produced by extensive mangrove stands and reed beds directly or indirectly via the food chains (Cha et al. 1997). Shrimps are repeatedly harvested from late spring to autumn by placing a funnel net into the partially opened sluice gate of a gei wai. As part of the management of Mai Po Marshes by WWFHK, the water level of gei wais is lowered during winter to help feed the tens of thousands of migratory water birds that roost at the RAMSAR site. Eventually, the ponds are completely drained in winter, commercial fish are harvested and after division into predatory and herbivorous species their biomass is estimated (Cha et al. 1997). In conclusion, the estimated fish production likely provides the most suitable data for InMANGROVE model calibration. However, for a coupling with the fish populations likely present in the simulated tidal channel, we also need to know the fish passage fraction either from video footing inside the sluice gate or from published meta analyses of guild-specific fish passage efficacy (Noonan et al. 2012, Hershey 2021).

Drift food concentration and search food concentration/replenishment constitute two major model parameters to which the IBM is very sensitive (Railsback et al. 2021). This represents another calibration issue. How do we obtain these parameters?

We considered the trophic model of Xu et al. (2011) for an intertidal mangrove-based polyculture system in the Pearl River Estuary to be an excellent source for these parameters. This was because the investigated polyculture system appeared to be very similar to the gei wais and, with common mullet and tilapia, two of the fish species encompassed by the trophic model of Xu et al. (2011) were also among the species being harvested in the gei wais (Cha et al. 1997).

Results

Work Package 1 (WP1) Juvenile fish use of small peri-urban mangroves

Eighteen species of fish were identified from our surveys in three mangrove patches. Fishes from two genera (*Gerres* and *Sillago*) and one family (Gobiidae) were unable to be identified to species level (Table 3). As expected, the video recordings performed better in more open mangrove patches in Ting Kok (TK), as two fishes there and Lai Chi Wo (LCW) were only encountered by this method. On the other hand, our traps were able to capture four

fishes in Shui Hau (SH) not seen in video recordings, as the turbid water in this site only allowed for sighting of fishes swimming very closely to the camera (<10 cm).

From our surveys, we concluded that two species of fish, *Ambassis gymnocephalus* (sub-adult to adult) and *Mugil cephalus* (juvenile) were abundant perennially and local populations would not be hurt by regular collection for ex-situ experiments. About 100-200 individuals of each species were taken back periodically to the marine science laboratory and were reared for the predation experiments.

Table 3. Fish species found in our field surveys. Each fish was identified to the most specific taxa possible. An asterisk (*) indicates taxa that were only encountered by video recording, while a caret (^) indicates taxa that were only caught by nets.

Family	Species	Location
Ambassidae	*Ambassis gymnocephalus*	LCW, SH, TK
Belonidae	*Strongylura strongylura*	TK
Carangidae	*Caranx ignobilis* ^	SH
Engraulidae	*Stolephorus* sp.	LCW
Gerreidae	*Gerres* spp.	SH, TK
Gobiidae	Unidentified species	LCW, SH, TK
Lutjanidae	*Lutjanus argentimaculatus* ^	SH
Mugilidae	*Mugil cephalus*	SH, TK
Siganidae	*Siganus canaliculatus* ^	SH
Sillaginidae	*Sillago* spp.	SH, TK
Sparidae	*Acanthopagrus latus* *	TK
	Acanthopagrus schlegelii ^	SH
Scatophagidae	*Scatophagus argus*	TK
Tetraodontidae	*Takifugu alboplumbeus*	LCW, SH, TK
Teraponidae	*Terapon jarbua*	LCW, SH, TK

Work Package 2 (WP2) Drivers for use of mangroves by juvenile fish

Analysis of 3D scanning methods

Three models from seven mangrove tree species and three methods were 3D scanned (n = 63) (Figure 27). We assessed each model's viability for 3D-printing and predation experiments by comparing their structural complexity metrics (Figure 27, Table 4). Both area/volume ratio and interstitial volume ratio were significantly different among mangrove tree species ($F_{6,56} = 34.11$, $p < 0.001$ and $F_{6,56} = 169.64$, $p < 0.001$, respectively) and methods ($F_{2,56} = 4.43$, $p = 0.017$ and $F_{2,56} = 32.87$, $p < 0.001$, respectively) (Table 5). Post hoc Tukey test revealed that only the Kinect and ZEB Revo produced significant difference from the measurement of area/volume ratio, while all methods were significantly different for the measurement of interstitial ratio (Table 6).

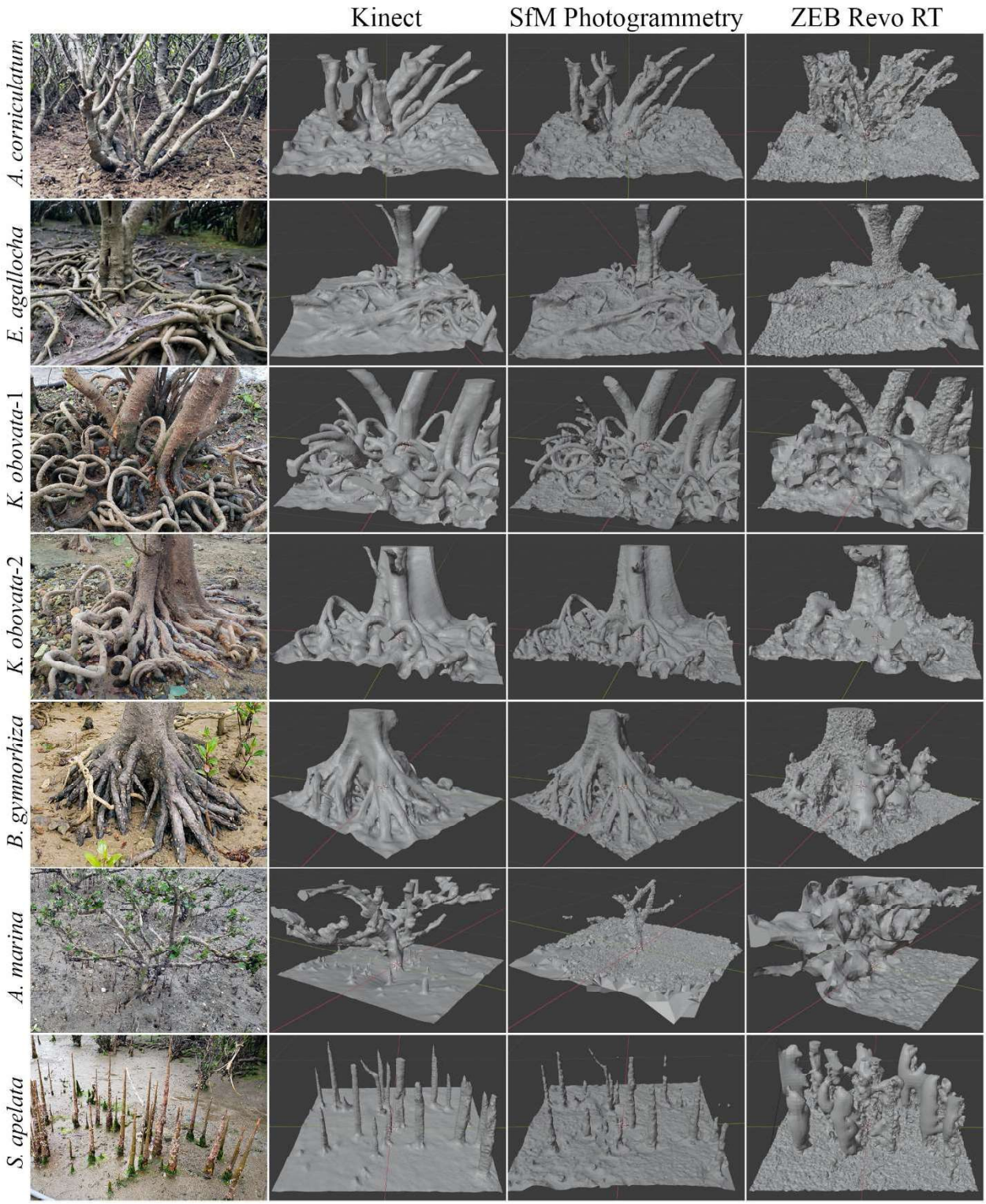

Figure 27. Comparison of scanned mangrove trees to their digital 3D models. Trees were chosen for scanning based on their structural complexity and accessibility. Each model was cropped into 1 m^2 in ground area.

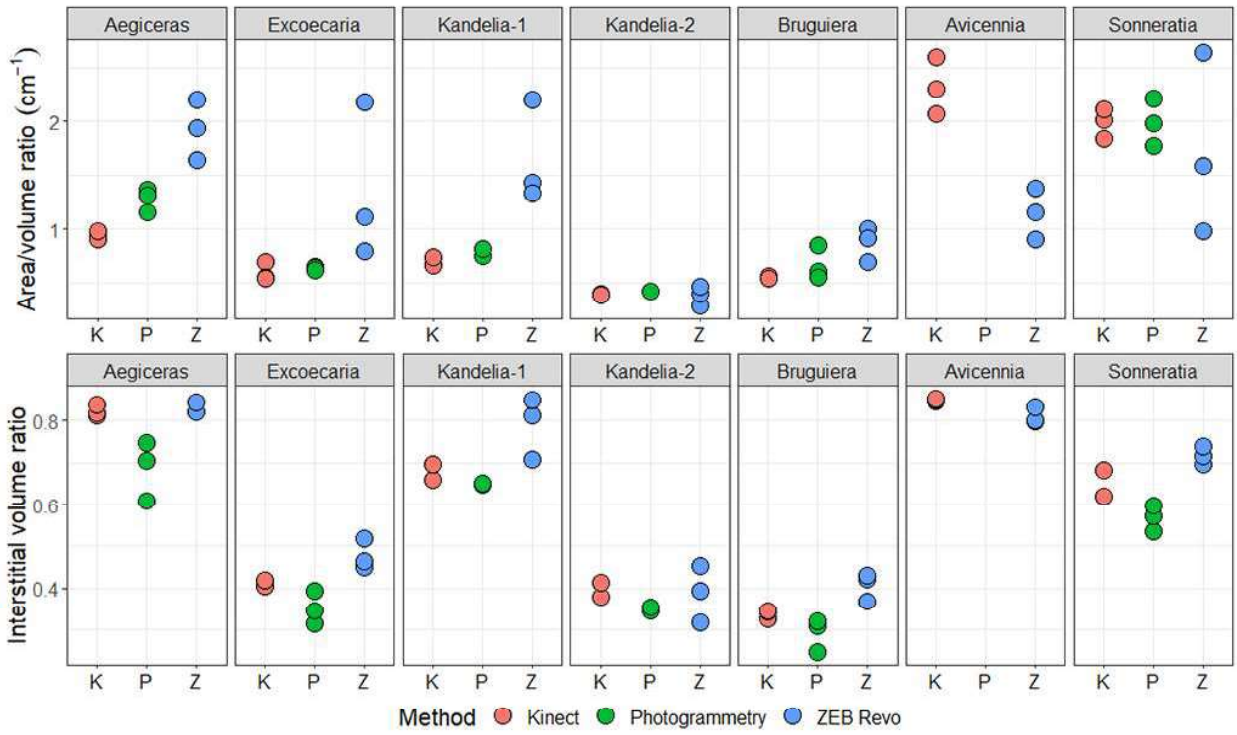

Figure 28. Area/volume ratio and interstitial volume ratio of all seven mangrove tree structures scanned using the Kinect (red), SfM photogrammetry (green), and ZEB Revo (blue). Both area/volume ratio and interstitial volume ratio were significantly different among species and scanning methods (see text for details).

Table 4. Volume, surface area, and structural complexity measurements from each mangrove tree structures scanned using three different methods.

Species	Method	Volume (cm^3)	Surface area (cm^2)	Area/volume ratio (cm^{-1})	Interstitial volume ratio
Aegiceras corniculatum	Kinect	25,823.6 ± 761.9	24,274.3 ± 308.5	0.94 ± 0.04	0.82 ± 0.01
	SfM photogrammetry	15,415.3 ± 2,192.5	19,546.0 ± 1,132.9	1.28 ± 0.11	0.69 ± 0.07
	ZEB Revo	19,119.4 ± 1,725.4	36,659.4 ± 4,795.0	1.93 ± 0.04	0.84 ± 0.01
Avicennia marina	Kinect	10,086.0 ± 1,621.3	23,144.0 ± 1,136.6	2.32 ± 0.26	0.85 ± 0.00
	SfM photogrammetry	-	-	-	-
	ZEB Revo	36,405.8 ± 7,917.1	41,791.7 ± 14,345.8	1.14 ± 0.23	0.81 ± 0.02
Bruguiera gymnorhiza	Kinect	57,161.3 ± 1,185.1	31,414.5 ± 1,154.6	0.55 ± 0.02	0.34 ± 0.01
	SfM photogrammetry	41,296.9 ± 7,604.0	26,952.5 ± 973.2	0.67 ± 0.16	0.29 ± 0.04
	ZEB Revo	63,867.9 ± 2,914.8	55,675.5 ± 11,563.5	0.87 ± 0.16	0.41 ± 0.03
Excoecaria agallocha	Kinect	33,075.9 ± 3,792.5	19,577.5 ± 341.0	0.60 ± 0.08	0.41 ± 0.01
	SfM photogrammetry	29,402.3 ± 1,760.1	18,697.0 ± 545.2	0.64 ± 0.02	0.35 ± 0.04
	ZEB Revo	31,391.6 ± 3,778.4	41,456.4 ± 18,735.1	1.36 ± 0.72	0.48 ± 0.04
Kandelia obovata-1	Kinect	55,833.9 ±2,283.2	38,481.7 ± 701.0	0.69 ± 0.04	0.67 ± 0.02
	SfM photogrammetry	41,636.8 ± 833.4	32,517.9 ± 1,200.2	0.78 ± 0.04	0.65 ± 0.00
	ZEB Revo	33,175.8 ± 8,631.3	52,351.1 ± 2,158.4	1.66 ± 0.47	0.79 ± 0.07
Kandelia obovata-2	Kinect	54,220.5 ± 723.9	21,367.8 ± 679.9	0.39 ± 0.01	0.40 ± 0.02
	SfM photogrammetry	49,770.1 ± 2,312.0	21,091.4 ± 926.1	0.42 ± 0.00	0.35 ± 0.01
	ZEB Revo	63,506.4 ± 11,374.5	23,805.6 ± 1,813.2	0.39 ± 0.09	0.39 ±0.07
Sonneratia apetala	Kinect	9,492.5 ± 1,036.5	18,776.0 ± 909.5	1.99 ± 0.14	0.66 ± 0.04
	SfM photogrammetry	7,277.6 ± 908.9	14,330.7 ± 394.9	1.99 ± 0.22	0.57 ± 0.03
	ZEB Revo	26,806.8 ± 14,207.1	39,000.0 ± 2,251.1	1.74 ± 0.84	0.72 ± 0.02

Table 5. ANOVA for the effects of species and method on area/volume ratio and interstitial volume ratio. Reciprocal transformation was applied on area/volume ratio dataset to fit it to a normal distribution prior to analyses.

Source of variation	DF	SS	MS	F	P
ANOVA: area/volume ratio					
Species	6	21.234	3.539	34.11	**<0.001**
Method	2	0.919	0.460	4.43	**0.017**
Residuals	48	4.980	0.104		
Total	56	26.869	0.480		
ANOVA: interstitial volume ratio					
Species	6	1.828	0.305	169.64	**<0.001**
Method	2	0.118	0.059	32.87	**<0.001**
Residuals	48	0.0862	0.0018		
Total	56	2.139	0.038		

Table 6. Post hoc Tukey test for the effects of scanning method on area/volume ratio and interstitial volume ratio. Reciprocal transformation was applied on the dataset to fit it on a normal distribution prior to analyses.

Comparison	Diff. of means	q	P	P<0.050
Tukey: area/volume ratio				
Kinect vs. Photogrammetry	0.112	1.435	0.571	No
Kinect vs. ZEB Revo	0.297	4.168	0.014	Yes
Photogrammetry vs. ZEB Revo	0.185	2.399	0.217	No
Tukey: interstitial volume ratio				
Kinect vs. Photogrammetry	0.0766	7.460	<0.001	Yes
Kinect vs. ZEB Revo	0.0393	4.190	0.013	Yes
Photogrammetry vs. ZEB Revo	0.116	11.417	<0.001	Yes

We calculated root mean square error (RMSE) and bias of tree circumference between the models and real trees to determine the accuracy and precision of each scanning technique. The Kinect scanned trees with an RMSE and bias of 1.64 cm (5.27%) and 0.35 cm (1.12%) respectively, SfM photogrammetry with 1.36 cm (3.65%) and 0.23 cm (0.57%) respectively, and ZEB Revo with 4.87 cm (14.70%) and 0.90 cm (2.70%) respectively (Figure 29). All

models except one were positively biased, which means that all 3D scanning methods tend to overestimate tree circumference. However, linear regression shows that all three methods could generate models with relatively accurate dimensions (Kinect, $y = 1.05x + 5.33$, $R^2 = 0.992$; SfM photogrammetry, $y = 1.12x - 1.04$, $R^2 = 0.990$; ZEB Revo, $y = 1.22x + 11.51$, $R^2 = 0.856$).

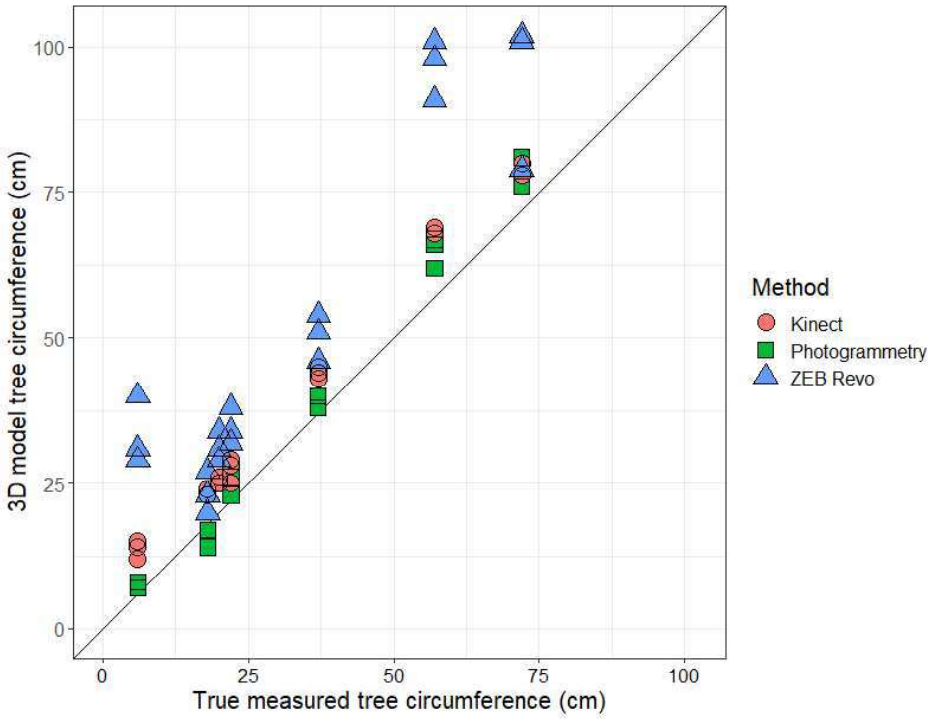

Figure 29. Accuracy of mangrove tree circumference estimation by three scanning methods. All methods overestimated tree circumference, except for *A. corniculatum* scanned by SfM photogrammetry. R^2 Kinect = 0.992; SfM photogrammetry = 0.990; ZEB Revo = 0.856. The straight line is the isometric line (1:1).

Of all three scanning methods, the Kinect was the only method to accurately scan the trees of all species and its models retained the highest number of intact branches and pneumatophores (Figure 27). However, positive bias in scanning results made several independent, but closely positioned tree structures (e.g., aerial roots of *Excoecaria agallocha* in Figure 30) fuse with each other and eliminated gaps and crevices shaped by these structures. In real mangrove trees, this framework of crevices forms important microhabitats and refuges for juvenile fishes and invertebrates by reducing the efficiency of larger predators (Kamal et al. 2014; Laegdsgaard and Johnson 2001; Primavera 1997). The under-representation of this important aspect of mangrove tree structures may disqualify the Kinect

models from being used for experiments regarding habitat use and animal behaviour at a small scale, but they may still be suitable for processes that occur at the meter-scale.

Figure 30. Close-up preview of *Excoecaria agallocha* models scanned using Kinect (left), SfM photogrammetry (center left and center right), and ZEB Revo (right). The model third from the left was opened with Window's built-in 3D Viewer software to show its color and texture, while the rest were previewed using Blender.

Moreover, the necessity of having a constant electrical supply and computer connection required researchers to carry an additional portable battery, cables and a water-resistant laptop computer that reduced their mobility in thick vegetation and uneven terrain. Working hours were also limited to overcast days, early morning (before 9 A.M.) and dusk (after 6 P.M.) to avoid direct sunlight heating and reflecting from tree surfaces. The 3D mesh, which was visible for real-time preview during the scanning routine, would quickly shrink and disintegrate under moderate sunlight. The sensitivity of the Kinect toward direct light was challenging for scanning of thin and condensed pneumatophores of *Avicennia marina* and *Sonneratia apetala*, which were most common in the open, lower shore section of a mangrove forest (Morton 2016). The scanned objects, as previewed on the laptop computer connected to the Kinect, would often disappear, or reduced to obsolete particles when the Kinect was moved too quickly. We therefore were only able to move the Kinect marginally from the starting position and had to restart the scanning routine for multiple times before obtaining consistent acceptable results.

Structure from motion (SfM) photogrammetry was relatively easy and affordable to use, as it required no equipment but one device for photo taking (e.g., a digital camera, or in this study, our personal smartphones) and a sizeable scale (e.g., one-meter-long PVC pipe lain down close to the mangrove trees). Meshroom's ability to detect and stitch photos in different lighting, as well as to augment finished models with additional photos allowed for a more flexible working time and a window for fixing errors. However, augmentation attempts

with photos too far apart in time (> 2 weeks) were likely to fail, as vegetations grow and surrounding environments change rapidly in the mangrove forest. Extra precaution was needed as SfM photogrammetry still suffered from repeatability issues, as multiple reconstructions made from the same set of pictures did not result in identical models (Napolitano and Glisic 2018). Hence, each model then had to be resized manually depending on the length of the physical scale lain near it (mean = 0.58 ± sd 0.22, n = 16) to match the sizes of the real trees. Manual adjustment to the model's dimensions may translate into errors made in scaling, rotation, and translation of the finished models (Carbonneau and Dietrich 2017). In addition, the models generated by SfM photogrammetry for trees with low canopies (*A. corniculatum* and *A. marina*) and thin pneumatophores (*A. marina* and *S. apetala*) often excluded many parts of these tree species, likely due to errors in the 'feature matching' and 'meshing' nodes of the reconstruction process. As many of the *A. marina* trees in Hong Kong start branching at under 50 cm, the resulting box-shaped models (dimension: 1 × 1 × 0.4 or 0.5 m) lacked any meaningful structures to be considered successful reconstructions, thus removed from further statistical analyses (Figure 27). A minor branch on the *E. agallocha* model was also absent from the SfM reconstruction (circumference = 7 cm).

Despite these issues, SfM photogrammetry was able to produce models with higher quality tree texture and depicted surface complexity more accurately than the Kinect (Figure 30). The results of circumference estimation outperformed the other two methods and even a past SfM photogrammetry study using potted plants (Miller et al. 2015, diameter at breast height RMSE: 9.6%; this study, circumference at base or at 50 cm RMSE: 3.7%). Although not statistically significant, area/volume ratios were slightly higher than that of the Kinect, as better textural quality translated into higher surface area (Figure 28, Table 6). Interstitial volume per available space was found to be lower than both the Kinect and ZEB Revo (Figure 28), which was likely the outcome of reduced shrinkwrap model sizes from missing branches of the top parts of the tree models. Photogrammetry also has the added advantage that it is applicable under water, so that spatially complex structures such as coral heads can theoretically be reconstructed using this method. Underwater scanning using Kinect or ZEB Revo is not possible.

GeoSLAM ZEB Revo RT was able to not only estimate mangrove tree circumference with acceptable accuracy, but also capture a significantly larger scanning area (about 10×) compared to the other two methods tested in this study. The drawback of this wide-range

scanning capabilities was apparent in the highly noisy point cloud output resulting from moving leaves, branches, and other small particles. These 'impurities' in the point cloud data were unavoidable while working outdoors, and they were persistent in the mesh subsequently generated by Poisson surface reconstruction (Figure 28). Even after extensive noise cleaning using CloudCompare's statistical outlier removal (SOR) filter (sigma = 1.00), the resulting mesh often came with 'bubbles' and unwanted additional vertices that hindered subsequent volume and area measurements. This outcome was highlighted in the lower precision of structural complexity measurements, especially the area/volume ratio of *A. marina*, *E. agallocha*, *K. obovata*-1, and *S. apetala* (Figure 28). The final mesh models did not sufficiently interpret the fine intricacies that were paramount in natural mangrove trees and were not suitable to be used in experiments related to structural complexities. Nevertheless, its ability to scan a large area in a short amount of time may prove useful in forest inventory, ground topology and rapid estimation of mangrove forest biomass and therefore, blue carbon storage, as have been highlighted by other studies in the past (Cabo et al. 2018; Del Perugia et al. 2019; Gollob et al. 2020; Potter 2019; Stal et al. 2020). However, the high cost of ZEB Revo (~40,000 USD), compared to the other two methods (~ 0 to 200 USD) may become an obstacle from wide usage in ecological research.

3D printing of mangrove structures

Based on the above considerations, we decided to use the models generated by SfM photogrammetry for 3D-printing, largely due to high precision and textural detail of their digital models. Three models were chosen for printing, which included one of *K. obovata* with 'complex' root structures (Figure 27, row 3; dimension = 1 × 0.9 × 0.7 m), one of *K. obovata* with 'simple' root structures (Figure 27, row 4; dimension = 1 × 1 × 0.9 m), and one of mixed *K. obovata* and *A. corniculatum* (dimension = 1 × 1 × 0.7 m) (Figure 31). These models were chosen due to a wide range of complexities of their root structures, indicated by their contrasting structural complexity metrics. These metrics change as we altered the water level in the experimental setup (Table 7). Area/volume ratio and interstitial volume ratio of both *K. obovata* models increase as water level decreases, reflecting the complexity of their root structures, while they reduce as water level decreases for the mixed model, reflecting the complexity of its widely-branching tree trunks. Total tree perimeter increases as water level decreases for all models.

Figure 31. **3D printed mangrove tree models**. Left: model one, high-complexity *K. obovata* tree; centre: model two, low-complexity *K. obovata* tree; and right: model three, *K. obovata* and *A. corniculatum* trees. Models are coated with a non-volatile, non-toxic, paint in a colour resembling natural tree surfaces.

Table 7. The physical attributes and structural complexities of mangrove models in three different water levels.

Model	Water lv. (cm)	Volume (cm^3)	Surface area (cm^2)	Perimeter (cm)	A/V ratio (cm^{-1})	IV ratio
Complex	60	52,448.84	36,639.38	95	0.70	0.65
Complex	40	32,977.04	34,153.02	116	1.04	0.71
Complex	25	27,099.57	31,802.73	199	1.17	0.87
Simple	60	41,709.88	23,718.12	64	0.57	0.36
Simple	40	36,799.21	22,278.70	79	0.61	0.40
Simple	25	32,566.16	21,007.97	94	0.65	0.47
Mixed	60	27,014.82	19,941.07	151	0.74	0.54
Mixed	40	25,909.21	18,243.58	165	0.70	0.50
Mixed	25	23,648.85	15,544.59	175	0.66	0.38

Predation experiments

In total, we have conducted 39 experiments using 13 predatory *Lutjanus argentimaculatus* with the complex and simple models. Out of 39 experiments, 27 were

conducted with 150 *Mugil cephalus,* 11 with 100 *Ambassis gymnocephalus*, and 1 with 15 *Terapon jarbua*. 15 experiments using *L. argentimaculatus* and *M. cephalus* were used for data analysis in this report. The remaining *M. cephalus* experimental results were not used in this report as we did not record any predatory activity, presumably due to behavioural changes influenced by prolonged captivity. For experiments with active predators, the number of chases and attacks did not differ significantly between the complex and simple models and between three water levels. However, there were significant differences in the percentage of preys eaten with varying water levels and the percentage of successful predation with varying models and water levels (Table 8; Figure 32).

Table 8. ANOVA for the effects of model and water level on number of chases, number of attacks, percentage of preys eaten, and percentage of successful predation events.

Source of variation	DF	SS	MS	F	P
ANOVA: number of chases					
Model	1	34.8	34.81	0.676	0.4286
Water level	2	334.8	167.39	3.249	0.0779
Residuals	11	566.8	51.53		
Total	14	936.4	253.73		
ANOVA: number of attacks					
Model	1	34.0	34.0	0.394	0.543
Water level	2	305.4	152.72	1.768	0.216
Residuals	11	950.3	86.39		
Total	14	1,289.7	273.11		
ANOVA: preys eaten					
Model	1	880	880	1.715	0.21701
Water level	2	8,157	4,079	7.945	**0.00733**
Residuals	11	5,647	513		
Total	14	14,684	5,472		
ANOVA: successful predation events					
Model	1	993	993.3	9.083	**0.0118**
Water level	2	5,667	2,833.7	25.913	**<0.001**
Residuals	11	1,203	109.4		
Total	14	7,863	3,936.4		

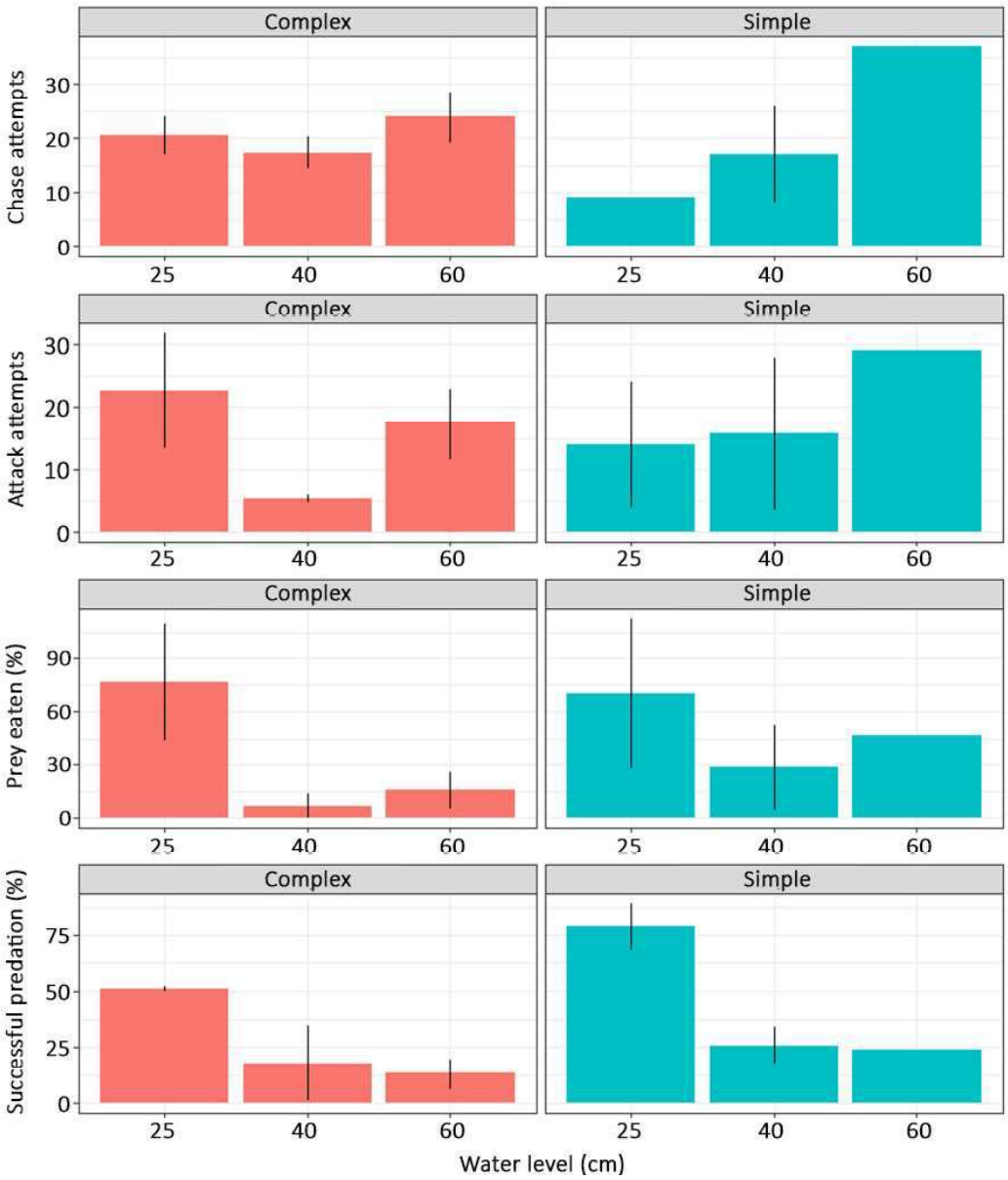

Figure 32. P**redatory events occurring between two models and three water levels** (n = 15).

Prior to predator introduction, prey mullets spent most time at the bottom (70.29 ± 21.97%) and middle (30.71 ± 25.03%) sections of the tank but migrated almost entirely to the top (96.88 ± 3.63%) of the tank after the introduction of predators (Figure 33). Surfacing allows prey mullets to maintain the farthest distance possible from predators, which spent most of their time at the bottom (59.72 ± 19.74%) and middle (38.44 ± 13.63%) sections of the tank, similar to the prey mullets prior to their introduction (Figure 33). Surfacing also allows stacks of guanine crystals in the subdermal layer of the 'silvery' fish skin to reflect light (Denton and Nicol 1965; Levy-Lior et al. 2008). Low-polarizing reflection of fish skins

is used a common anti-predator mechanism by many pelagic teleost fishes, such as clupeids (e.g., sardines, herrings, and sprats in Jordan et al. 2012), as well as *M. cephalus* and *A. gymnocephalus* used in this study. The prey fish likely surfaced to use the sunlight from above to conceal their location and movements from the predators below them.

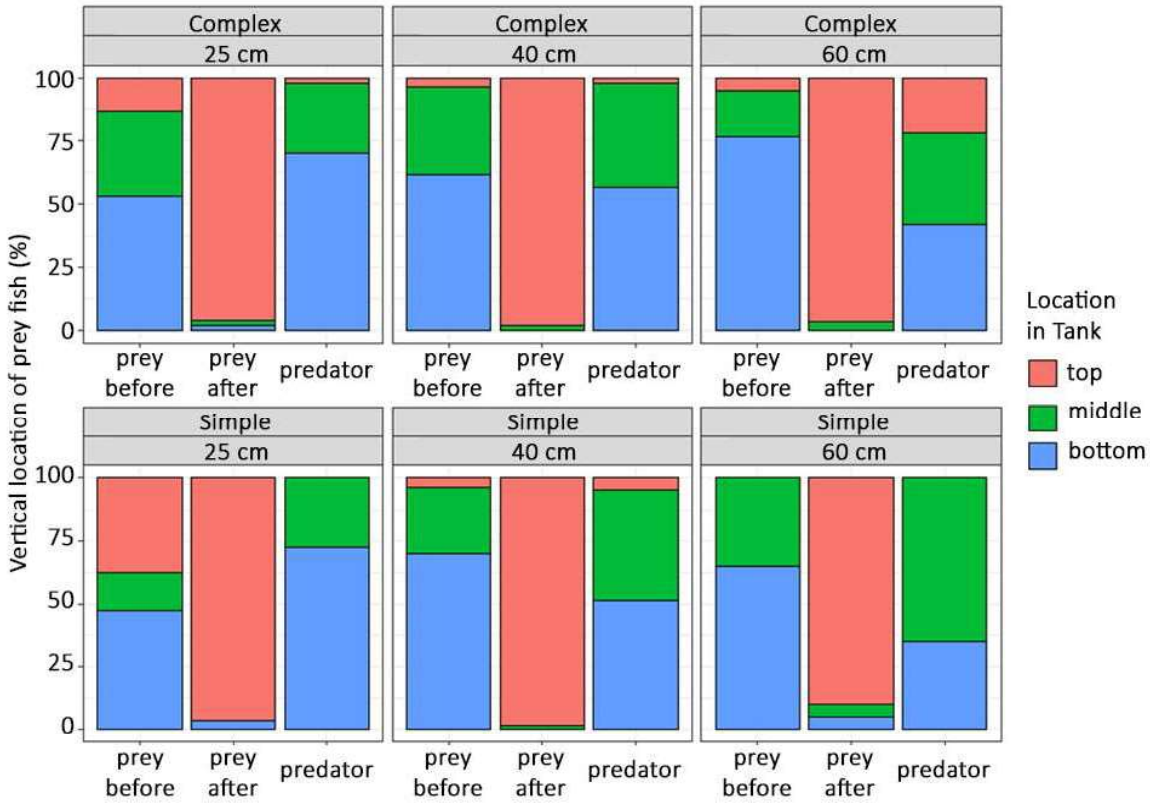

Figure 33. **Vertical location of prey fish** before and after predator introduction and predators during the experiments. 'prey before' data was collected on the first half of the experiment, while 'prey after' and 'predator' were taken on the second half.

While surfacing allows prey fish to avoid detection and escape predation attempts, it greatly reduced the contact between the prey fish and tree models, as the tree roots were located at the bottom section of the models (Figure 31). Therefore, surfacing prey fish only came into contact with the sections of the model touching the water surface, which only included the outer perimeter of the largest tree trunks at water levels 40 and 60 cm, but included some of the models' looping aerial roots at 25 cm (Table 8). Water level showed a significant correlation to prey mullet's increased tendency to swim inside the mangrove model (Figure 31; one-way ANOVA, $F = 4.163$, $p = 0.0244$). At 25 cm, prey mullets utilized the models more frequently by swimming and stopping between crevices, probably because these structures were within reach at this water level. At higher water levels, prey fish were

most often seen aggregating and swimming in groups, and would only stop and hide at the tank's edges. Grazing behaviours were only observed prior to predator introduction, when the prey mullets were less alert and would swim at the bottom of the tank.

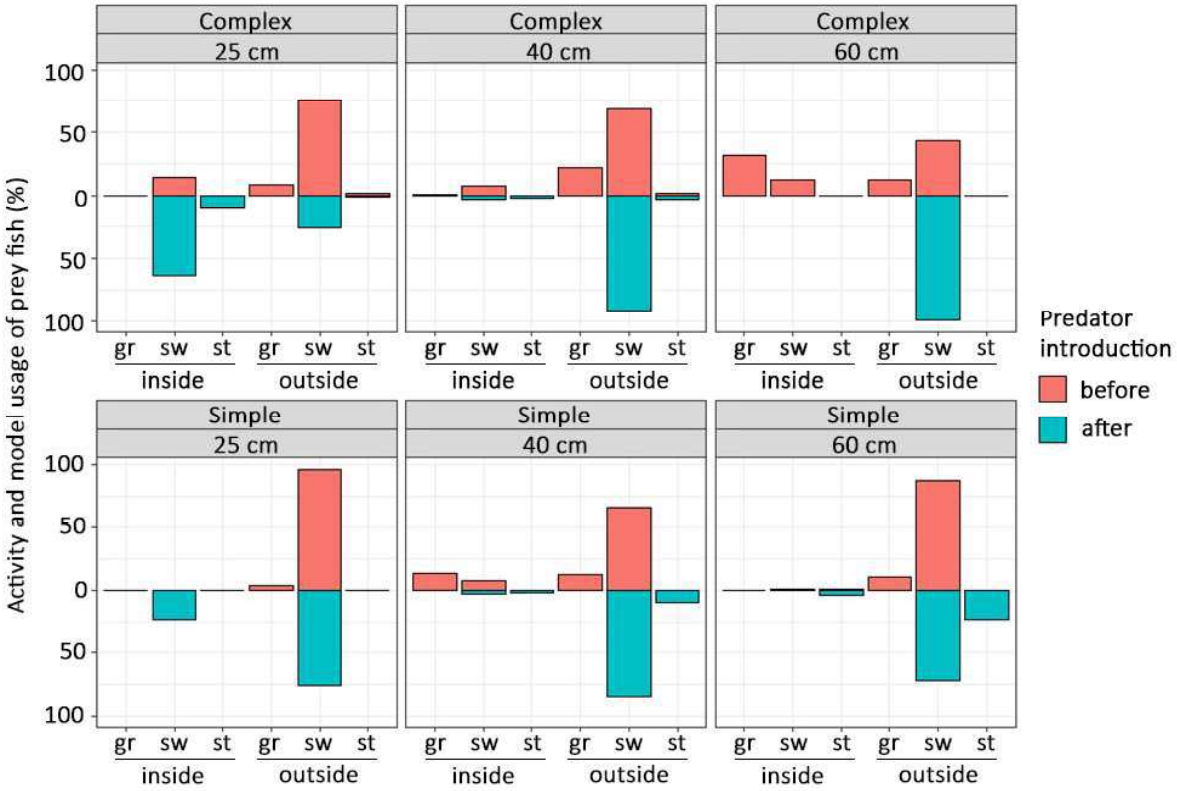

Figure 34. Prey activity and usage of mangrove model before and after predator introduction. 'gr': grazing, 'sw': swimming, 'st': stopping (hiding).

While the prey mullets spent the majority of their time schooling (Figure 34), the variety of swimming patterns exerted showed various strategies critical for prey survival (Figure 32). Schooling was the most common behaviour observed, both before and after predator introduction. Without the presence of predators, a group of mullets would form a loose group at the bottom of the tank, often breaking into two or more separate groups to either swim or graze in the surrounding areas. Movements during this period were often haphazard, patterns were irregular, and collective vision was not focused at one direction. This type of social behaviour may function to increase the probability of detecting food and achieve a maximum rate of energy intake (de Carvalho et al. 2007). On the other hand, with the presence of predators, the group ceased grazing behaviours, immediately ascended, and formed a tight school. This school would move in a coordinated fashion and swim faster against the location of the predators. When they were not being pursued, they would fixate

their vision toward the predator, and swim in a zig-zagging pattern (swaying left and right but maintaining zero displacement) (Figure 35). Schooling during a period of perceived danger may provide the prey mullets several antipredator properties, such as confusion effect, dilution of risk, predator detection, and risk abatement (Krakauer 1995; Handegard et al. 2012).

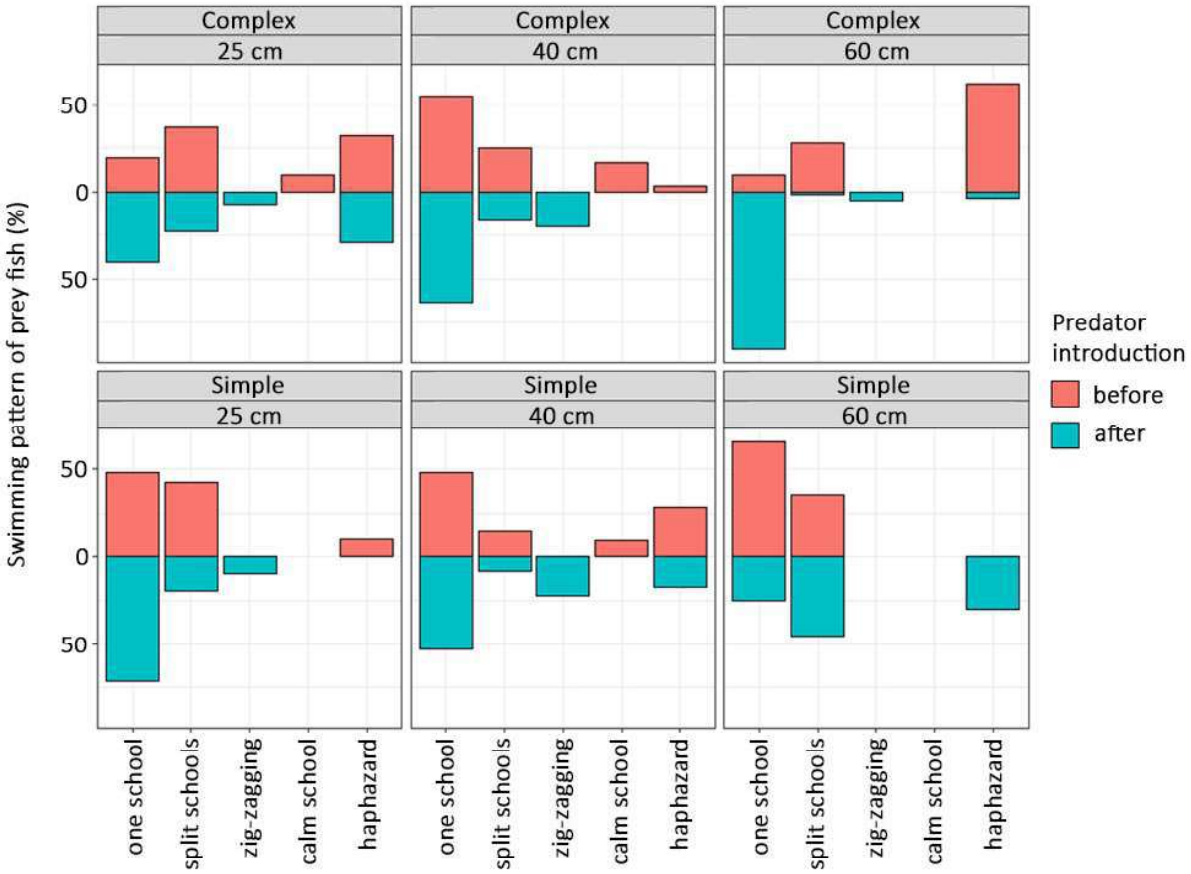

Figure 35. **Prey swimming and grouping patterns** before and after predator introduction.

Interestingly, water level also showed a significant correlation to the predators swimming inside (Figure 33; one-way ANOVA, $F = 7.058$, $p = 0.018$) and stopping inside (one-way ANOVA. $F = 6.297$, $p = 0.0241$) the mangrove models. The predators were observed to conceal themselves within the models and shift their colours darker to match the model's shade prior to ambushing the prey fish. As the number of prey eaten and successful predation attempts were higher at lower water level (Figure 31), ambushing from within the models may be more successful when the time needed is shorter to swim toward the water surface, where the prey fish were at (Figure 33). As surfacing and schooling provided the prey mullets benefits for survival, ambushing allowed the predators to decrease spatial

coherence within schools and increase fragmentation to break them into easier targets (Handegard et al. 2012).

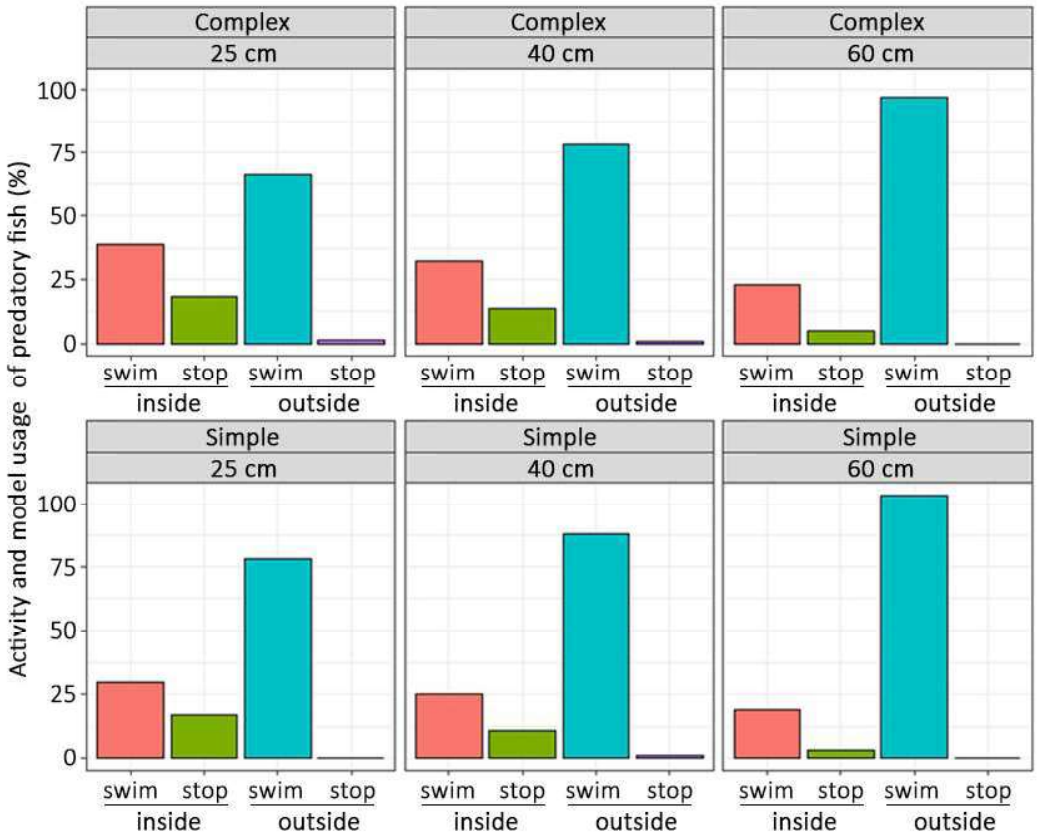

Figure 36. Predator activity and usage of mangrove model.

Overall, these sets of novel experiments demonstrated the feasibility of using 3D-printed models to observe predator-prey interactions in small-scale mangrove settings. While natural habitats are often ridden with obstacles, such as the rarity of predation events, water turbidity, and changeable tidal cycle, 3D printing has allowed us to monitor predation events in a controlled and replicable environment. Here, we showed that spatial complexity benefitted both prey fish and predators by providing refuge for reducing detection rates. Moreover, tidal cycles, mimicked by the manipulation of water levels, influenced fish behaviour and the effectivity of the mangrove models.

Work Package 3 (WP3) Individual-based modelling of juvenile use of mangroves

Presentation: The graphical user interface (GUI) of the InMANGROVE model

At present, the InMangroveModelWithUI (with the GUI) is started by pressing the Run button inside the Eclipse Integrated Development Environment. Information about the executed start-up processes is printed out on the Eclipse console.

Figure 37 shows the model GUI that appears when the start-up is complete. Initially, the "About" pane comprising the InMANGROVE-IBM logo is presented. The logo contains an image of bald glassy perchlets (*Ambassis gymnocephalus*) swimming among the 3D-printed *Kandelia obovata* prop roots in the aquarium experiments. A second image shows a view from the Hong Kong Wetland Park being part of the Mai Po Marshes. The logo includes the names of the investigators in the project and MEEF as the funding organization.
The other panes that the user can activate are the "Console", "Displays & Charts" and the "Model" (Parameters) pane.

A second window, empty at first, opens in the background. When the Initialize button of the GUI is pressed, the 2D Display of the site to be simulated, here the study site at the Mai Po Nature Reserve, is loaded into this window. Figure 38 presents a screenshot of the 2D Display.

Various charts of fish abundance dynamics and fish eggs counts over time can be set visible, separately or altogether, via the GUI's "Displays & Charts" pane. Figure 39 provides an overview of all the available charts.

Outlook: Continuation of the modeling work until mid-February 2022 is agreed upon. It is planned to complete the implementation of the mangrove rooting systems, the derivation of the rating curves for the hydraulics and the model calibration for one or more fish species.

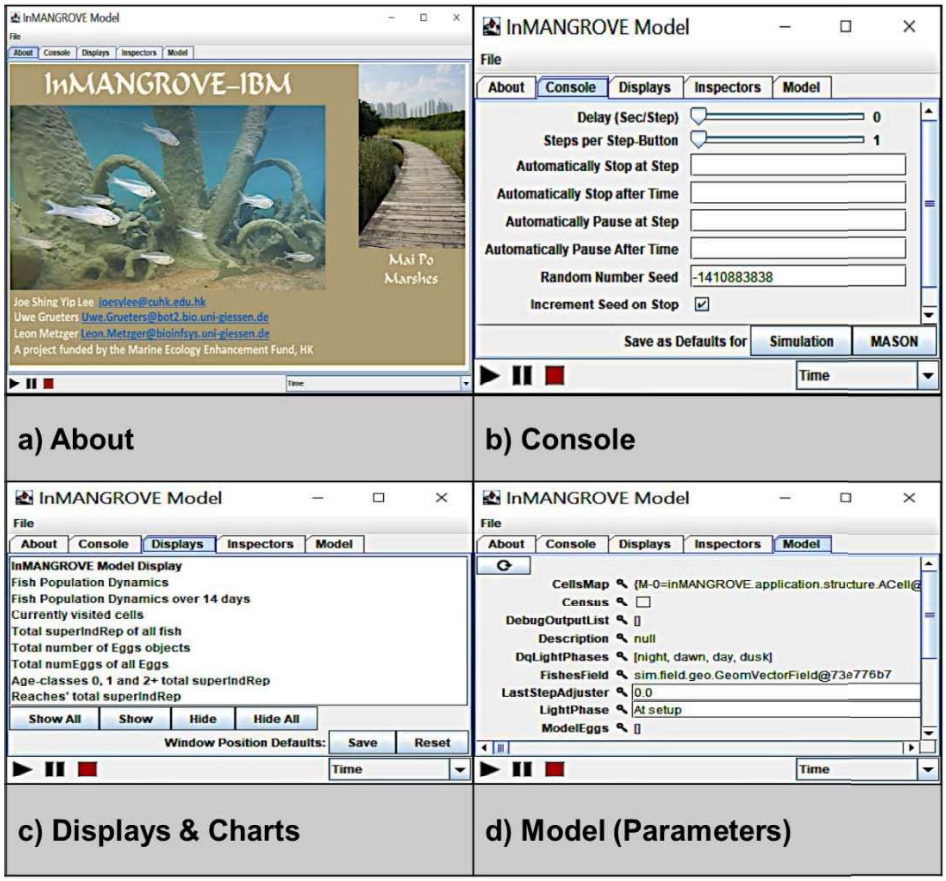

Figure 37. The Graphical User Interface of the InMANGROVE model with a) the "About" pane, b) the "Console" pane, c) the "Displays & Charts" pane and d) the "Model" pane

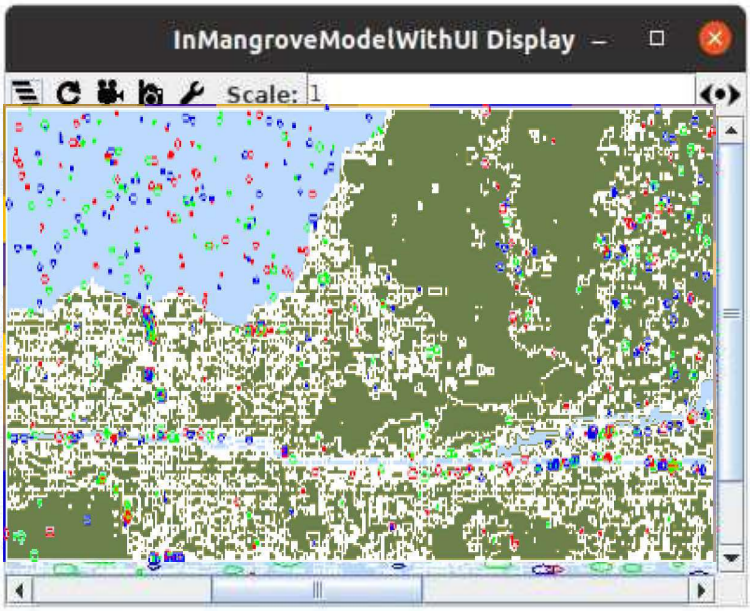

Figure 38. 2D Display of the InMANGROVE-IBM

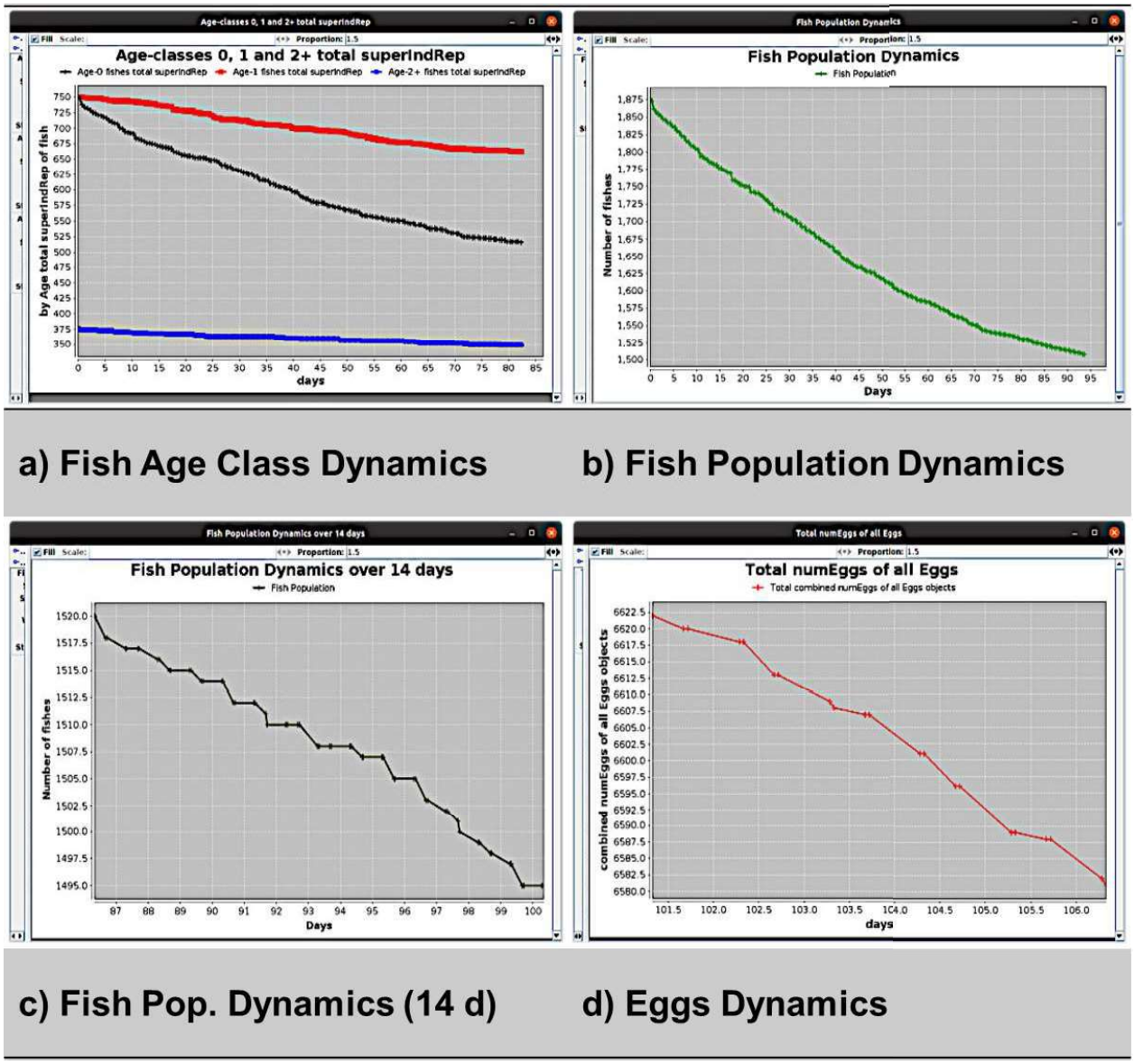

Figure 39. **Overview of the charts available in the model**

Outlook

Despite the central achievements being made during the project period, considerable effort and work in terms of implementing the mangrove structural complexity and rating curves as well as calibration for local fish species will be needed to complete the individual-based model. Further work will also be necessary for the application of the InMANGROVE model to promote the nursery function of the mangrove forest in the Mai Po Nature Reserve. This initial model development, however, has laid the foundation to detailed modelling of the use of small mangrove forests by juvenile fish.

Acknowledgments

The project team would like to thank the members of the Lee Mangrove Lab for their continuous support throughout this study, particularly Rinaldi Gotama, Jubilee Kwong, Ip Tsz Yu, and Bianca Leung. The following staff of the Chinese University of Hong Kong are thanked for assistance with various components of this project: Mr. Barry Tai, Ms Phyllis Yau, Ms Yvonne Chan, Ms Belin Chow, Ms Alice Poon, and Ms Kenus Wu; as well as Ms Jolene Wong and Tiffany Tsang of ERM-MEEF. This study was supported by grants (2019002, 2019002A) from the Marine Ecology Enhancement Fund, Hong Kong.

Ethics statement

Ex-situ predation experiments with live vertebrates were endorsed by Hong Kong's Department of Health [Ref. Nos.: (20-373), (20-374), and (20-375) in DH/HT&A/8/2/1 Pt. 7 for Lee Shing Yip, Kwong Hei Nin, and Gotama Rinaldi, respectively, and (20-612) and (20-613) in DH/HT&A/8/2/1 Pt. 21 for Leung Sum Yin and Ip Tsz Yu, respectively] and CUHK's Animal Experimentation Ethics Committee (Ref. No.: 20-139-MEF).

Outreach and Dissemination of Project Outcomes

Student training

We have been training two CUHK students to conduct predation experiments as their Final Year Projects (FYP). Their results will be disseminated as a presentation and report, which will be due in May 2022. The FYP students working on this project are as follows:

- Leung Sum Yin, August – December 2021.
- Ip Tsz Yu, August 2021 – present.

Conference presentations (* = main presenter)

Lee S. Y.*, Gotama R., Kwong H. N., Grüters U. Value of peri-urban and small-scale mangrove forests in the Pearl River Estuary as fish habitats. Marine Ecological Enhancement Fund public meeting. November 2021.

Gotama R.*, Kwong H. N., Lee S. Y. Comparison of 3D-scanning techniques for digital reconstruction of mangrove tree structures. 1st International Symposium on Marine Science and Engineering for Young Scientists and Postgraduates. The Hong Kong University of Science and Technology, Hong Kong SAR, China (online). 12th – 14th July 2021.

Publications

Gotama R., Kwong H. N., Lee S. Y. (in revision) Comparison of 3D scanning techniques for digital reproduction of mangrove tree structures. Submitted to *Limnology & Oceanography: Methods.*

Timetable

Completion of the various project milestones:

Project task	Planned completion date	Actual completion date
Finalise funding agreement with JLU	April 2021	April 2021
Recruitment and commencement of SRA	April – May 2021	April – May 2021
Mesocosm experiments using 3D printed structures	April – June 2021	April – December 2021
Individual-based modelling of fish use of mangrove roots	May – October 2021	May – December 2021
Data analysis, preparation of reports and other outputs	October – December 2021	October – December 2021
Submission of Completion Report	January 2022	February 2022

Declaration

"I hereby irrevocably declare to the MEEF Management Committee and the Steering Committee of the relevant Funds including the Top-up Fund, that all the dataset and information included in the completion report has been properly referenced, and necessary authorisation has been obtained in respect of information owned by third parties."

Any opinions, findings, conclusions or recommendations expressed in this report do not necessarily reflect the views of the Marine Ecology Enhancement Fund or the Trustee.

Prof. Joe S.Y. Lee, Principal Investigator

References

Alongi DM (2009) The energetics of mangrove forests. Springer, New York. pp.216.

Arcement GJ and Schneider VR (1989) Guide for Selecting Manning's Guide for Selecting Manning's Roughness Coefficients for Natural Channels and Flood Plains. . U.S. Geological Survey,

Ayllon D, Railsback SF, Vincenzi S, Groeneveld J, Almodovar A and Grimm V (2016) InSTREAM-Gen: Modelling eco-evolutionary dynamics of trout populations under anthropogenic environmental change. Ecological Modelling 326:36-53.

Bi HQ (2004) Stochastic frontier analysis of a classic self-thinning experiment. Austral Ecology 29:408-417.

Bogetoft P and Otto L (2011) Benchmarking with DEA, SFA, and R. Springer, New York.

Botkin DB, Janak JF and Wallis JR (1972) Rationale, Limitations, and Assumptions of a Northeastern Forest Growth Simulator. Ibm Journal of Research and Development 16:101-&.

Brooker RM, Seyfferth AL, Hunter A, Sneed JM, Dixson DL and Hay ME (2020) Human proximity suppresses fish recruitment by altering mangrove-associated odour cues. Scientific Reports 10:

Cabo C, Del Pozo S, Rodriguez-Gonzalvez P, Ordonez C and Gonzalez-Aguilera D (2018) Comparing Terrestrial Laser Scanning (TLS) and Wearable Laser Scanning (WLS) for Individual Tree Modeling at Plot Level. Remote Sensing 10:

Cao JJ, Liu K, Zhuo L, Liu L, Zhu YH and Peng LH (2021) Combining UAV-based hyperspectral and LiDAR data for mangrove species classification using the rotation forest algorithm. International Journal of Applied Earth Observation and Geoinformation 102:

Carbonneau PE and Dietrich JT (2017) Cost-effective non-metric photogrammetry from consumer-grade sUAS: implications for direct georeferencing of structure from motion photogrammetry. Earth Surface Processes and Landforms 42:473-486.

Castaneda-Moya E, Twilley RR, Rivera-Monroy VH, Marx BD, Coronado-Molina C and Ewe SML (2011) Patterns of Root Dynamics in Mangrove Forests Along Environmental Gradients in the Florida Coastal Everglades, USA. Ecosystems 14:1178-1195.

Cha MW, Young L and Wong KM (1997) The fate of traditional extensive (gei wai) shrimp farming at the Mai Po Marshes Nature Reserve, Hong Kong. Hydrobiologia 352:295-303.

Chan PK, Ching SH and Erftemeijer P (2011) Developing a Mangrove Management Strategy in the Estuaries of Deep Bay, Shan Pui River and Tin Shui Wai Drainage Channel. . In: (ed.) CIWEM HK Water Conference 2011: Advanced Technologies and Practices in Water Management, Hong KongVolume: Proceedings.

Curnick DJ, Pettorelli N, Amir AA, Balke T, Barbier EB, Crooks S, Dahdouh-Guebas F, Duncan C, Endsor C, Friess DA, Quarto A, Zinmer M and Lee SY (2019) The value of small mangrove patches. Science 363:239-239.

de Carvalho CD, Corneta CM and Uieda VS (2007) Schooling behavior of *Mugil curema* (Perciformes: Mugilidae) in an estuary in southeastern Brazil. Neotropical Ichthyology 5:81-83.

de la Moriniere EC, Nagelkerken I, van der Meij H and van der Velde G (2004) What attracts juvenile coral reef fish to mangroves: habitat complexity or shade? Marine Biology 144:139-145.

Del Perugia B, Giannetti F, Chirici G and Travaglini D (2019) Influence of scan density on the estimation of single-tree attributes by hand-held mobile laser scanning Forests 10:277.
Denton EJ and Nicol JAC (1965) Polarization of light reflected from the silvery exterior of the bleak, *Alburnus alburnus* Journal of the Marine Biological Association of the United Kingdom 45:705-709.
Duke NC and Khan MA (1999) Structure and composition of the seaward mangrove forest at the Mai Po Marshes Nature Reserve, Hong Kong. pp.83-104. In: Lee SY (ed.) The Mangrove Ecosystem of Deep Bay and the Mai Po Marshes, Hong Kong. Hong Kong University Press, Hong Kong.
FAO (2007) The World's Mangroves: 1980-2005. FAO, Rome, Italy. pp.89.
Gamma E (1995) Design patterns. Elements of reusable object-oriented software Addison-Wesley, Reading, MA, USA.
Gedan KB, Altieri AH, I. F, R. B and D. B (2017) Community composition in mangrove ponds with pulsed hypoxic and acidified conditions. . Ecosphere 8:e02053.
Gollob C, Ritter T and Nothdurft A (2020) Forest inventory with long range and high-speed personal laser scanning (PLS) and simultaneous localization and mapping (SLAM) technology. Remote Sensing 12:
Grimm V and Railsback SF (2005) Individual-based modeling and ecology. . Princeton University Press, Princeton. pp.428.
Grueters U, Ibrahim MR, Schmidt H, Tiebel K, Horn H, Pranchai A, Vovides AG, Vogt J, Otero V, Satyanarayana B and Dahdouh-Guebas F (2021) Stable Coexistence in a Field-Calibrated Individual-Based Model of Mangrove Forest Dynamics Caused by Inter-Specific Crown Plasticity. Forests 12:
Guo XX, Wang M, Jia MM and Wang WQ (2021) Estimating mangrove leaf area index based on red-edge vegetation indices: A comparison among UAV, WorldView-2 and Sentinel-2 imagery. International Journal of Applied Earth Observation and Geoinformation 103:
Gutierrez-Heredia L, D'Helft C and Reynaud EG (2015) Simple methods for interactive 3D modeling, measurements, and digital databases of coral skeletons. Limnology and Oceanography-Methods 13:178-193.
Handegard NO, Boswell KM, Ioannou CC, Leblanc SP, Tjøstheim DB and Couzin ID (2012) The dynamics of coordinated group hunting and collective information transfer among schooling prey. Current Biology 22:1213-1217.
Hershey H (2021) Updating the consensus on fishway efficiency: A meta-analysis. Fish and Fisheries 22:735-748.
Hoque ARM, Sharma S and Hagihara A (2011) Above and belowground carbon acquisition of mangrove Kandelia obovata trees in Manko Wetland, Okinawa, Japan. International Journal of Environment 1:7-13.
Horstman EM, Bryan KR, Mullarney JC, Pilditch CA and Eager CA (2018) Are flow-vegetation interactions well represented by mimics? A case study of mangrove pneumatophores. Advances in Water Resources 111:360-371.
Huijbers CM, Mollee EM and Nagelkerken I (2008) Post-larval French grunts (*Haemulon flavolineatum*) distinguish between seagrass, mangrove and coral reef water: Implications for recognition of potential nursery habitats. Journal of Experimental Marine Biology and Ecology 357:134-139.
Jia MM, Zhang YZ, Wang ZM, Song KS and Ren CY (2014) Mapping the distribution of mangrove species in the Core Zone of Mai Po Marshes Nature Reserve, Hong Kong, using hyperspectral data and high-resolution data. International Journal of Applied Earth Observation and Geoinformation 33:226-231.

Jia MM, Liu MY, Wang ZM, Mao DH, Ren CY and Cui HS (2016) Evaluating the effectiveness of conservation on mangroves: a remote sensing-based comparison for two adjacent protected areas in Shenzhen and Hong Kong, China. Remote Sensing 8:
Jordan TM, Partridge JC and Roberts NW (2012) Non-polarizing broadband multilayer reflectors in fish. Nature Photonics 6:759-763.
Kamal S, Lee SY and Warnken J (2014) Investigating three-dimensional mesoscale habitat complexity and its ecological implications using low-cost RGB-D sensor technology. Methods in Ecology and Evolution 5:845-853.
Kamal S, Warnken J, Bakhtiyari M and Lee SY (2017) Sediment distribution in shallow estuaries at fine scale: in situ evidence of the effects of three-dimensional structural complexity of mangrove pneumatophores. Hydrobiologia 803:121-132.
Kowalik Z and Luick J (2019) Modern Theory and Practice of Tide Analysis and Tidal Power. . Austides Consulting, Eden Hills, South Australia, Australia.
Krakauer DC (1995) Groups confuse predators by exploiting perceptual bottlenecks: a connectionist model of the confusion effect. Behavioural Ecology and Sociobiology 36:421–429.
Laegdsgaard P and Johnson CR (1995) Mangrove habitats as nurseries - unique assemblages of juvenile fish in subtropical mangroves in eastern Australia. Marine Ecology-Progress Series 126:67-81.
Laegdsgaard P and Johnson C (2001) Why do juvenile fish utilise mangrove habitats? Journal of Experimental Marine Biology and Ecology 257:229-253.
Lee SY, Primavera JH, Dahdouh-Guebas F, McKee K, Bosire JO, Cannicci S, Diele K, Fromard F, Koedam N, Marchand C, Mendelssohn I, Mukherjee N and Record S (2014) Ecological role and services of tropical mangrove ecosystems: a reassessment. Global Ecology and Biogeography 23:726-743.
Lee SY (2022) Repairing Hong Kong estuaries: challenges and prospects. In: Waltham N (ed.) Repairing the World's Estuaries: Knowledge, Challenges and the Necessary Success Ahead. Elsevier, Oxford.
Levy-Lior A, Pokroy B, Levavi-Sivan B, Leiserowitz L, Weiner S and Addadi L (2008) Biogenic guanine crystals from the skin of fish may be designed to enhance light reflectance. Crystal Growth and Design 8:507-511.
Li HZ, Han Y and Chen JS (2020) Combination of Google Earth imagery and Sentinel-2 data for mangrove species mapping. Journal of Applied Remote Sensing 14:
Li QS, Wong FKK and Fung T (2019) Classification of Mangrove Species Using Combined WordView-3 and LiDAR Data in Mai Po Nature Reserve, Hong Kong. Remote Sensing 11:
Liu K, Li X, Shi X and Wang SG (2008) Monitoring mangrove forest changes using remote sensing and GIS data with decision-tree learning. Wetlands 28:336-346.
Liu MF, Zhang HS, Lin GH, Lin H and Tang DL (2018) Zonation and directional dynamics of mangrove forests derived from time-series satellite imagery in Mai Po, Hong Kong. Sustainability 10:
Manson FJ, Loneragan NR, Harch BD, Skilleter GA and Williams L (2005) A broad-scale analysis of links between coastal fisheries production and mangrove extent: A case-study for northeastern Australia. Fisheries Research 74:69-85.
Mazda Y, Wolanski E, King B, Sase A, Ohtsuka D and Magi M (1997) Drag force due to vegetation in mangrove swamps. . Mangroves and Salt Marshes 1:193–199.
Meynecke JO, Lee SY and Duke NC (2008) Linking spatial metrics and fish catch reveals the importance of coastal wetland connectivity to inshore fisheries in Queensland, Australia. Biological Conservation 141:981-996.

Miller J, Morgenroth J and Gomez C (2015) 3D modelling of individual trees using a handheld camera: Accuracy of height, diameter and volume estimates. Urban Forestry & Urban Greening 14:932-940.
Monsi M and Saeki T (1953) Über den Lichtfaktor in den Pflanzengesellschaften und seine Bedeutung für die Stoffproduktion. . Japanese Journal of Botany 14:22 − 52.
Morton B (2016) Hong Kong's mangrove biodiversity and its conservation within the context of a southern Chinese megalopolis. A review and a proposal for Lai Chi Wo to be designated as a World Heritage Site. Regional Studies in Marine Science 8:382-399.
Muñoz DF, Yin DX, Bakhtyar R, Moftakhari H, Xue Z, Mandli K and Ferreira C (2021) Inter-model comparison of Delft3D-FM and 2D HEC-RAS for total water level prediction in coastal to inland transition zones. Journal of the American Water Resources Association JAWR-20-0114-P
Nagelkerken I, Blaber SJM, Bouillon S, Green P, Haywood M, Kirton LG, Meynecke JO, Pawlik J, Penrose HM, Sasekumar A and Somerfield PJ (2008) The habitat function of mangroves for terrestrial and marine fauna: A review. Aquatic Botany 89:155-185.
Nagelkerken I (2009) Evaluation of nursery function of mangroves and seagrass beds for tropical decapods and reef fishes: patterns and underlying mechanisms. pp.357-399. In: Nagelkerken I (ed.) Ecological Connectivity among Tropical Coastal Ecosystems.
Nagelkerken I, De Schryver AM, Verweij MC, Dahdouh-Guebas F, van der Velde G and Koedam N (2010) Differences in root architecture influence attraction of fishes to mangroves: A field experiment mimicking roots of different length, orientation, and complexity. Journal of Experimental Marine Biology and Ecology 396:27-34.
Napolitano RK and Glisic B (2018) Minimizing the adverse effects of bias and low repeatability precision in photogrammetry software through statistical analysis. . J. Cult. Herit. 31:46-52.
Natin P and Lee SY (2018) Estuarine caridean shrimp (*Palaemon debilis* Dana, 1852) (Decapoda: Caridea) can differentiate olfactory cues from different mangrove species for microhabitat selection. Journal of Experimental Marine Biology and Ecology 501:99-108.
Noonan MJ, Grant JWA and Jackson CD (2012) A quantitative assessment of fish passage efficiency. Fish and Fisheries 13:450-464.
Potter TL (2019) Mobile laser scanning in forests: Mapping beneath the canopy. Ph.D. thesis University of Leicester.
Pretzsch H and Biber P (2005) A re-evaluation of Reineke's rule and stand density index. Forest Science 51:304-320.
Primavera JH (1997) Fish predation on mangrove-associated penaeids - The role of structures and substrate. Journal of Experimental Marine Biology and Ecology 215:205-216.
R Development Core Team (2012) R: A language and environment for statistical computing. http://www.R-project.org,
Railsback SF, Lamberson RH, Harvey BC and Duffy WE (1999) Movement rules for individual-based models of stream fish. Ecological Modelling 123:73-89.
Railsback SF, Harvey BC and Ayllón D (2021) InSTREAM 7 User Manual: Model Description, Software Guide, and Application Guide. . pp.273.
Reichert J, Schellenberg J, Schubert P and Wilke T (2016) 3D scanning as a highly precise, reproducible, and minimally invasive method for surface area and volume measurements of scleractinian corals. Limnology and Oceanography-Methods 14:518-526.
Reineke LH (1933) Perfecting a stand-density index for even-aged forests. . U.S. G.P.O, Washington D.C., USA.

Richards DR and Friess DA (2016) Rates and drivers of mangrove deforestation in Southeast Asia, 2000-2012. Proceedings of the National Academy of Sciences of the United States of America 113:344-349.
Robertson AI and Duke NC (1990a) Recruitment, growth and residence time of fishes in a tropical Australian mangrove system. Estuarine Coastal and Shelf Science 31:723-743.
Robertson AI and Duke NC (1990b) Mangrove fish-communities in tropical Queensland, Australia - spatial and temporal patterns in densities, biomass and community structure. Marine Biology 104:369-379.
Sheaves M, Johnston R and Abrantes K (2007) Fish fauna of dry tropical and subtropical estuarine floodplain wetlands. Marine and Freshwater Research 58:931-943.
Sheaves M, Baker R, Nagelkerken I and Connolly RM (2015) True value of estuarine and coastal nurseries for fish: incorporating complexity and dynamics. Estuaries and Coasts 38:401-414.
Shugart HH (1984) A theory of forest dynamics. The ecological implications of forest succession models. . Springer-Verlag,, New York. pp.278.
Stal C, Verbeurgt J, De Sloover L and De Wulf A (2020) Assessment of handheld mobile terrestrial laser scanning for estimating tree parameters. J. For. Res.
UNEP (2014) The importance of mangroves to people: a call to action. UNEP World Conservation Centre, Cambridge, UK.
Vorsatz LD, Pattrick P and Porri F (2021) Quantifying the in situ 3-dimensional structural complexity of mangrove tree root systems: Biotic and abiotic implications at the microhabitat scale. Ecological Indicators 121:
Wang G, Guan DS, Zhang QP, Peart MR, Chen YJ, Peng YS and Ling X (2014) Spatial patterns of biomass and soil attributes in an estuarine mangrove forest (Yingluo Bay, South China). European Journal of Forest Research 133:993-1005.
Weiskittel A, Gould P and Temesgen H (2009) Sources of variation in the self-thinning boundary line for three species with varying levels of shade tolerance. Forest Science 55:84-93.
Xu SN, Chen ZZ, Li CH, Huang XP and Li SY (2011) Assessing the carrying capacity of tilapia in an intertidal mangrove-based polyculture system of Pearl River Delta, China. Ecological Modelling 222:846-856.
Young L (1999) Distribution of mangrove species in the intertidal zone at the Mai Po Marshes Nature Reserve. pp.117-130. In: Lee SY (ed.) The Mangrove Ecosystems of Deep Bay and the Mai Po Marshes, Hong Kong. Hong Kong University Press, Hong Kong.
Zhang YS, Xiao L, Guan DS, Chen YJ, Motelica-Heino M, Peng YS and Lee SY (2021) The role of mangrove fine root production and decomposition on soil organic carbon component ratios. Ecological Indicators 125:107525.
Zhu LF, Wu Q, Dai JY, Zhang SN and Wei FW (2011) Evidence of cellulose metabolism by the giant panda gut microbiome. Proceedings of the National Academy of Sciences of the United States of America 108:17714-17719.

Appendices

Appendix A: Audited Statement of Accounts

Details of financial statement are not disclosed due to confidentiality reasons.

Appendix B: List of Project Assets (funded under project MEEF2019002)

List of project assets is not disclosed due to confidentiality reasons.

Appendix C: Staff Attendance Records

Staff attendance record is not disclosed due to confidentiality reasons.

"I hereby irrevocably declare, warrant and undertake to the MEEF Management Committee and the Steering Committee of the relevant Funds including the Top-up Fund, that I myself, and the Organisation:-

1. *do not deal with, and are not in any way associated with, any country or organisation or activity which is or may potentially be relevant to, or targeted by, sanctions administered by the United Nations Security Council, the European Union, Her Majesty's Treasury-United Kingdom, the United States Department of the Treasury's Office of Foreign Assets Control, or the Hong Kong Monetary Authority, or any sanctions law applicable;*

2. *have not used any money obtained from the Marine Ecology Enhancement Fund or the related Top-up Fund (and any derived surplus), in any unlawful manner, whether involving bribery, money-laundering, terrorism or infringement of any international or local law; and*

3. *have used the funds received (and any derived surplus) solely for the studies or projects which further the MEEF Objectives and have not distributed any portion of such funds (including any derived surplus) to members of the Recipient Organisation or the public."*

Signed:

Professor Joe S Y Lee (Principal Investigator)

16 March 2022